

Analysis of Lithium-Ion Battery State and Degradation via Physicochemical Cell and SEI Modeling

Daniel Witt,^[a, b, d] Fridolin Röder,^[c] and Ulrike Krewer^{*[a]}

The quality of lithium-ion batteries is affected by the formation of the solid electrolyte interphase (SEI). For a better understanding of its effect on cell performance and aging, fast and economically scalable SEI diagnostics are indispensable. Battery models promise to extract hardly accessible interfacial and bulk properties of the SEI from electrochemical impedance spectra and discharge data. The common analysis of only one measurement, often with empirical models, impedes a precise localization of degradation-related and performance-limiting proc-

esses. This work offers a solution by combining physicochemical SEI and cell modeling for the joint analysis of both measurement types. Our analysis highlights the minor importance of the SEI ionic conductivity for cell performance along with a significant improvement and notable effect of its interfacial properties along aging. Such a detailed understanding of the initial SEI and its evolution over time could enable, e.g., a knowledge-based optimization of the cell formation process.

Introduction

The state of health of a lithium-ion battery can be evaluated by various criteria like its capacity loss^[1] or its change in internal resistance.^[2] However, these metrics inextricably summarize the effects of likely different underlying changes at the electrode and particle levels. Simulation studies can be used proactively to develop cell designs with reduced mechanical stress in the active material,^[3] to identify the impact of electrode manufacturing uncertainties on cell performance,^[4] and to recommend application-specific electrode configurations, e.g., to prevent detrimental lithium plating during fast charging.^[5] The prediction of the actual cell degradation remains an intricate challenge of lithium-ion battery technology, which is still too complex for predictive first principle aging models without extensive experimental data.^[6,7] Advanced model-based cell diagnostics can help to improve the understanding of fundamental degradation-related and performance-limiting processes. These insights can then be used to introduce knowledge-based electrode design and production process

adjustments, which are expected to be the main drivers for short-term cost and cycle life improvements.^[8]

For a holistic cell diagnosis, the solid electrolyte interphase (SEI) is of special importance as it affects both cell performance and degradation characteristics.^[9,10] It forms during the first cycles of a lithium-ion battery, predominately on the anode side. Essentially, the initial formation of the SEI suppresses its own growth and is key to a stable battery system. However, the composition, thickness, and structure of the SEI are not static after the initial formation. When electrochemically less stable SEI components degrade or when soluble components dissolve in the electrolyte, interfacial and bulk properties of the SEI can change.^[11] In addition, the breathing of the active material during cycling can trigger fractures in the SEI, promoting additional SEI growth.^[12] As a result, the formation of an initial SEI with favorable mechanical, chemical, interfacial, and conductive properties is of significant interest. The substantial process duration for its initial formation during battery production^[13] is another strong incentive for a detailed SEI characterization to enable knowledge-based process optimizations.

Available approaches for the characterization of the SEI can be divided into two categories: direct experimental and model-assisted approaches. Direct experimental techniques like transmission electron microscopy^[14] and X-ray photoelectron spectroscopy^[15] are related to significant preparative effort. Furthermore, these methods are commonly performed post-mortem, which complicates their utilization for broad experimental studies.

Model-assisted approaches can provide insights into the current cell and SEI state based on non-destructive electrochemical experiments like C-rate tests or electrochemical impedance spectroscopy (EIS) measurements. In principle, a cell diagnosis with a physicochemical lithium-ion battery model could describe and thus exploit a wide range of electrochemical measurements for a detailed cell state estimation. However, most models focus only on one measurement data

[a] D. Witt, Prof. U. Krewer
Institute for Applied Materials – Electrochemical Technologies, Karlsruhe
Institute of Technology, Adenauerring 20b, 76131, Karlsruhe, Germany
E-mail: ulrike.krewer@kit.edu

[b] D. Witt
Institute of Energy and Process Systems Engineering, TU Braunschweig,
Langer Kamp 19b, 38106 Braunschweig, Germany

[c] Prof. F. Röder
Bavarian Center for Battery Technology (BayBatt), Universitätsstraße 30,
95447 Bayreuth, Germany

[d] D. Witt
Battery LabFactory Braunschweig, TU Braunschweig, Langer Kamp 8, 38106
Braunschweig, Germany

Supporting information for this article is available on the WWW under
<https://doi.org/10.1002/batt.202200067>

© 2022 The Authors. Batteries & Supercaps published by Wiley-VCH GmbH.
This is an open access article under the terms of the Creative Commons
Attribution License, which permits use, distribution and reproduction in any
medium, provided the original work is properly cited.

type like C-rate test^[16,17] or EIS measurement.^[18,19] Such a restricted diagnosis is disadvantageous for multiple reasons. For example, a double-layer capacitance is likely better identifiable from EIS measurements than C-rate tests, whereas a solid diffusion coefficient may be better accessible from discharge curves.^[20,21] Importantly, there are also parameters like reaction rate constants that influence both C-rate and EIS data. Without a model for the joint analysis of both measurement types, a robust and unambiguous cell diagnosis cannot be ensured.^[20,22] Furthermore, SEI-related insights from aging models that use only cycling data^[17,23] are commonly limited to the loss of cyclable lithium, which is attributed to SEI growth. With an EIS-based cell state estimation, changes in interfacial SEI properties like process kinetics and double-layer capacitance become accessible.^[18] However, the interrelation with the discharge behavior remains unclear.

Apart from physicochemical models like single particle models,^[18] equivalent circuit models (ECM) have been widely used for impedance analysis and also system control due to their easily adjustable level of complexity and low computational cost.^[24,25] Nonetheless, with the goal of an in-depth cell state and aging understanding, a physicochemical model is preferred for two main reasons. First, it enables a straightforward physical interpretation of limiting processes and process changes. Second, it features a better extrapolation capability as a result of the modeling of physicochemical processes rather than the imitation of the cell behavior with electric circuits. Some publications combine the computational efficiency of ECMs with the insight of physicochemical models, though the employed approximations limit their scope to the analysis of EIS data.^[19,26] However, the complete translation of a physicochemical model into a spatially resolved ECM would allow to reproduce also dynamic charge and discharge measurements while offering physically meaningful parameter estimates.^[27]

Until now, the benefit of the joint analysis of EIS and discharge measurements with a cell model that comprises a detailed SEI modeling has not been investigated. We are going to demonstrate that an SEI-extended cell model can reproduce both measurements and provide detailed insights into the initial cell state after formation with clear changes in SEI and cell properties during aging. In future studies, this assignment of behavioral changes to physically meaningful parameters can help to advance cell and material design or even operating strategies for the mitigation of premature cell degradation.

The paper is divided into five major sections. First, the understanding and modeling of processes at the interfaces of the SEI as well as charge transport through the SEI are discussed. Subsequently, the chosen cell modeling framework is introduced, which builds the foundation for the following integration of the SEI model. Afterwards, an iterative model parameterization strategy is described, which exploits parameter sensitivities in different measurements for meaningful parameter estimates. In the next step, our experimental aging study is introduced. It provides the data for the final application of our concept to gain model-based insights into the initial cell state and its changes during aging. Here, we will reveal

changes in SEI properties and further aging-related cell parameters.

SEI Understanding and Modeling

To allow for an insightful modeling of the SEI that adds value to model-based cell diagnostics, a good understanding of its properties and transport mechanisms as well as its interfacial processes is crucial. An et al., Peled and Menkin, and Wang et al. provide comprehensive reviews on the SEI, covering aspects like its initial formation,^[11] current and future challenges of SEI-dependent battery systems,^[9] and relevant modeling approaches.^[28] It is generally accepted that the SEI is a complex composite structure, built of various degradation products with different electrochemical and mechanical stability as well as different transport properties. Here, inorganic products like Li_2CO_3 and LiF form a dense layer on the active material surface, which is covered by a porous organic outer layer. Organic SEI components are commonly less stable and undergo further reductions more easily, but they can create a better overall mechanical strength.^[29] For the modeling of the SEI, its multi-component nature along with its multi-layer structure raise fundamental questions about the optimal level of detail for model-based cell diagnostics. Furthermore, processes and reactions at the interfaces of the SEI as well as lithium-ion transport between them must be considered.

It is still under discussion whether a porosity of the SEI should be considered. Single et al. proposed a continuum model for the electrochemical formation of the SEI on graphite.^[30] Based on the suggested competition between electron conduction and solvent diffusion, a non-zero SEI porosity was predicted. Li et al. investigated the SEI on a lithium metal anode in a detailed simulation study.^[31] It is pointed out that only the inner layer of the anode surface film, i.e., the densely packed inorganic layer, should be considered as an effective passivation film that prevents further side reactions. The outer porous layer is not considered passivating due to liquid electrolyte in its pores. In this work, we will model only the dense inner layer of the surface film, which will be referred to as the SEI for simplicity.

Apart from the multi-layered structure of the SEI, it must be decided on the modeling of its multi-component nature. There are two archetypes of component alignment: serial connection and parallel connection. Obviously, a two-layer structure with one ionically almost isolating component like LiF on top of a better conductive component like Li_2CO_3 would result into a different overall transport loss compared to a side-by-side arrangement. Based on simple EIS measurements and C-rate tests, an insightful deconvolution of the overall SEI-related transport losses into individual SEI components along with information about their average alignment throughout the anode is unrealistic. Significant synergistic effects between components with individually unfavorable transport characteristics add a further level of complexity and uncertainty.^[32] In view of these two aspects, i.e., component orientation in the film and synergistic effects, an explicit modeling of the local SEI

properties would necessitate complex ex-situ measurements to reveal the local arrangement of different SEI components. Nonetheless, experimental limitations would still leave some questions open, e.g., regarding the effect of SEI morphology and composition on ion transport.^[33] Considering the desired SEI characterization based on fast and non-destructive measurements, we use an effective SEI ionic conductivity in this work.

In the following, charge transfer at the SEI interfaces, lithium-ion transport between the electrolyte and the active material phase, and the potential profile over the SEI thickness are discussed. Models on SEI-related cell degradation often consider only the ohmic properties of the SEI while using a classic Butler-Volmer expression for the intercalation reaction.^[17,23] To enable an accurate representation of cell dynamics and thus be able to simulate realistic impedance spectra, a more differentiated look at the involved reaction mechanism is necessary. In this context, Lück and Latz presented a model for an electrochemical double-layer between a planar electrode and a liquid electrolyte, which was used for the study of intercalation reactions.^[34,35] Based on experimental observations from lithium-ion batteries, they considered a two-step intercalation mechanism that comprises i) the lithium-ion de-/adsorption at the interface between solid and electrolyte phase, and ii) the de-/intercalation into the active material. For simplicity, they projected the spatial resolution of the double-layer on the interface between electrode and electrolyte. The interface was coupled to the transport in bulk electrode and bulk electrolyte. They concluded that the charging of the electrochemical double-layer is the driving force for charge transfer across the interface. However, this work did not yet consider a surface film between the active material and the electrolyte phase.

In our previous work, continuum pseudo two-dimensional (P2D) cell modeling and a kinetic Monte Carlo method were combined to analyze the growth of the SEI during cell formation.^[36] Here, lithium-ion transport through the SEI was described as a combination of three process steps: i) adsorption of a solvated lithium-ion at the interface of the SEI with the liquid electrolyte, ii) transport through the SEI to its inner interface, and iii) intercalation into the active material. Heinrich et al. used a similar setup for the analysis of impedance spectra along cell aging.^[18] Both studies assumed single ion conductor properties for the SEI, i.e., pure ionic conduction. For the sake of model simplicity, the transfer of an adsorbed lithium-ion into the SEI and its intercalation into the active material were treated as a homogeneous multi-step reaction.^[18,36,37] In this work, we adopt the three-step charge transfer mechanism from our previous work, but we consider the three steps individually rather than lumped together. Individual electrochemical double-layers as well as species balances are considered for both SEI interfaces.^[18,36] This is similar to the closed-form ECM-based impedance model by Kong et al., but we do not consider an additional interface between active material and electrolyte in parallel with the SEI.^[26]

Regarding transport through the SEI, the assumption of a single ion conductor is well supported by research. For

instance, Borodin et al. investigated lithium-ion transport in dilithium ethylene dicarbonate, Li₂EDC, which is a common organic SEI component.^[38] They suggested that Li₂EDC acts as a single ion conductor. Shi et al. used density functional theory to reveal the mechanism of lithium-ion transport in the inorganic SEI component Li₂CO₃.^[39,40] They suggested that lithium-ions are transported rapidly by pore diffusion in the porous outer organic SEI layer and by knock-off diffusion, i.e., displacement of neighboring lattice sites rather than direct-hopping through empty spaces, of interstitial Li⁺ in the inner inorganic SEI layer. They confirmed their results with estimated SEI resistances from impedance data as well as other measurements like TEM, XPS, and TOF-SIMS. With only one main diffusion carrier, this also points at a single ion conductor behavior. From the perspective of impedance modeling, Single et al. also investigated transport within the SEI.^[19] In a first step, they modeled it similar to transport in the electrolyte phase with both migration and diffusion. In the next step, they parameterized their model with experimental data. Here, they could only reproduce the experimental impedance spectra accurately with a transference number close to one, supporting the assumption of a single ion conductor behavior. However, the investigated symmetric cell with planar lithium metal electrodes, i.e., non-intercalation electrodes, and a Li-TFSI electrolyte in a tetraglyme solution may not be directly comparable to state-of-the-art lithium-ion batteries with graphite-based anodes. For this reason, we will keep the diffusion process in our model to assess its necessity for the reproduction of experimental EIS and C-rate data. We adopt the estimated SEI transference number of 0.97 from Single et al.^[19]

Figure 1 shows the translation of the discussed SEI understanding into a schematic representation of the SEI model, which we implement. It shows one representative anode active material particle covered by an SEI within a P2D cell model. The relevant processes and the potential profile through the SEI are shown. Henceforth, the interface between active material particle and SEI is indicated by the index sSEI; the interface between SEI and electrolyte is indicated by the index SEIe.

Model Development

With the ambition of fast, yet in-depth model-based cell diagnostics, the choice of an adequate cell modeling framework is crucial. This necessitates two fundamental trade-offs: i) Necessary model complexity for accurate reproduction of experimental data vs. computational effort. ii) Desired in-depth physicochemical insights vs. a potentially larger number of hardly identifiable model parameters.

Equivalent circuit models are commonly used for the analysis of electrochemical impedance spectra, but they can also be used to describe a cell's charge/discharge behavior.^[24,25,41,42] Still, ECMs rely on state of charge (SOC) dependent resistances that would need to be translated into diffusion coefficients or reaction rate constants for a detailed understanding of cell behavior changes. Physicochemical models directly describe the underlying processes like diffusion,

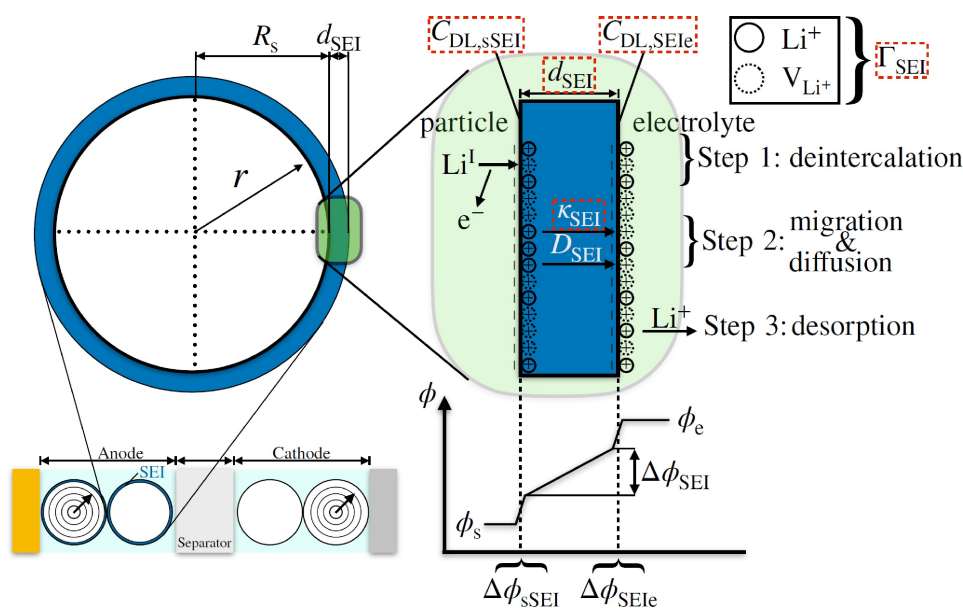


Figure 1. Graphical summary of the SEI model for the anode side, illustrating the potential profile at the interfaces of the SEI with electrochemical double-layers at both interfaces. The arrows at the magnified SEI on the right side indicate the pathway of a lithium-ion from the solid into the electrolyte phase. This comprises the deintercalation from the active material, the transport through the SEI to the active material-SEI (sSEI) interface via diffusion and migration, and the final desorption at the SEI-electrolyte (SEIe) interface. Furthermore, the surface sites and thus the electrochemical double-layers are shown with a non-zero spatial expansion, which would be expected in reality. However, in the model, this spatial resolution is eliminated, resulting into a potential-step at the interfaces. Finally, SEI-related parameters that are updated along cell aging in this work, are surrounded by dashed, red boxes.

migration, and concentration-dependent reaction kinetics. At the lower end of the complexity range, single particle models can be used for the analysis of quasi-steady state data, i.e., low C-rates and EIS.^[18,43] 3D microstructure-resolved battery models are likely to capture the electrochemical cell behavior best.^[44] However, their computational effort currently still prohibits their utilization for cell diagnostics. Furthermore, the measurement of the electrode microstructure, e.g., via synchrotron^[45] or FIB/SEM tomography^[46] results into additional effort and infrastructure requirements. The P2D model^[47] comes with the promise to resemble the model accuracy of a microstructure-resolved model with moderate computational cost. Here, the consideration of a particle size distribution would improve the model accuracy, but also increase the computational effort.^[44] As a result, we use a P2D modeling framework with one representative particle size for each electrode as the basis for the SEI modeling. Nonetheless, future advances in available computational power and the utilization of surrogate modeling^[48] could make microstructure-resolved battery models a great extension of the here presented SEI modeling.

In the following sections, the P2D cell model itself and the implementation of the SEI into this model are discussed in detail. In the end, the considered dynamics at the anode and cathode current collector are briefly described.

Basic P2D cell modeling framework

The model in this paper is based on the physicochemical P2D battery model as introduced by Doyle et al.^[47] It is extended by an electrochemical double-layer as proposed by Legrand et al. to enable meaningful EIS simulations.^[49] A summary of the basic equations for lithium-ion transport in the active material particles, in the electrolyte phase, and transfer between these phases is given in Table SI-1. The kinetics on the anode side are described with non-ideal activities.^[50,51] The detailed equations are provided in the following section. The kinetics on the cathode side are described with a Butler-Volmer expression, which represents a single rate-limiting process. For the concentration-dependent exchange current density, the activities in the active material and the electrolyte phase are obtained by normalization of the lithium-ion concentrations to the maximum solid concentration and the reference electrolyte concentration, respectively. A summary of these and other complementary model equations is given in Table SI-2 along with a schematic structure of the utilized P2D cell model in Figure SI-1. The modeling of the illustrated anode-side SEI is discussed in the following sections. Due to less pronounced and typically not performance-limiting surface film formation on the cathode side, this electrode is modeled SEI-free.^[52,53]

Implementation of the SEI in a P2D cell model

This section addresses the implications of a second interface between active material and electrolyte for the determination of the solid as well as electrolyte phase potential. Afterwards, the equations for the intercalation reaction, the adsorption process, and the transport through the SEI are introduced. Finally, the necessary equations for the potentials at the two electrochemical double-layers of the SEI as well as its interfacial surface coverages are shown.

The original Doyle-Fuller-Newman model does not consider a surface film between active material and electrolyte phase. Without the SEI, the solution of the solid phase potential ϕ_s and electrolyte phase potential ϕ_e at the location x within the cell is straightforward. With the electrochemical double-layer between solid and electrolyte phase, the total volumetric current of lithium-ions j^{tot} from electric conduction in the active material

$$j^{\text{tot}}(x) = \frac{\partial}{\partial x} \left[\sigma_{s,\text{eff}} \frac{\partial \phi_s(x)}{\partial x} \right] \quad (1)$$

with conductivity $\sigma_{s,\text{eff}}$ can be equated with the total lithium-ion current from migration and diffusion in the electrolyte phase

$$j^{\text{tot}}(x) = -\frac{\partial}{\partial x} \left[\sigma_{e,\text{eff}}(x) \frac{\partial \phi_e(x)}{\partial x} \right] - \frac{\partial}{\partial x} \left[\sigma_{\text{De,eff}}(x) \frac{\partial \ln(c_e(x))}{\partial x} \right] \quad (2)$$

with the ionic electrolyte conductivity $\sigma_{e,\text{eff}}$, the effective diffusive ionic conductivity $\sigma_{\text{De,eff}}$, and the electrolyte concentration $c_e(x)$. A numerical solution to this problem can be obtained with the finite volume method. In the classical P2D model, the desired potentials ϕ_s and ϕ_e can be obtained via the electrochemical potential at the double-layer

$$\Delta\phi^{\text{DL}} = \phi_s - \phi_e. \quad (3)$$

In an SEI-extended P2D cell model, the two SEI interfaces with their individual electrochemical double-layers result into a total of four instead of two relevant potentials. As a starting point, the potentials at the double-layers at both the inner and the outer SEI interface, i.e., $\Delta\phi_{s/\text{sSEI}}$ and $\Delta\phi_{\text{sSEI}/e}$, are initialized at the equilibrium potential of the active material vs. Li/Li⁺ and 0 V vs. Li/Li⁺, respectively. Then, the potential difference between solid and electrolyte phase can be expressed as

$$\phi_s - \phi_e = \Delta\phi_{s/\text{sSEI}} + \Delta\phi_{\text{sSEI}} + \Delta\phi_{\text{sSEI}/e} \quad (4)$$

with the potential drop $\Delta\phi_{\text{sSEI}}$ over the SEI thickness. The charge transport through the SEI is described with the Nernst-Planck equation^[54] according to

$$j^{\text{tot}} = \frac{\kappa_{\text{SEI}}}{a_s d_{\text{SEI}}} \left(\frac{RT(1 - 2t_{p,\text{SEI}})}{F} \ln \left(\frac{\theta_{\text{sSEI}}}{\theta_{\text{SEI}/e}} \right) - \Delta\phi_{\text{sSEI}} \right) \quad (5)$$

with the SEI ionic conductivity κ_{SEI} , the specific surface area a_s of the spherical active material particles, the universal gas constant R , the temperature T , the transference number in the SEI $t_{p,\text{SEI}}$, the Faraday constant F , the interfacial lithium-ion coverage at the inner and outer interface of the SEI θ_{sSEI} and $\theta_{\text{SEI}/e}$, respectively, and the SEI thickness d_{SEI} . In combination with Equations (1) and (2), this allows for the calculation of the total volumetric lithium-ion current in presence of the SEI along with the corresponding solid and electrolyte phase potential.

In the following, all equations for lithium-ion transport and transfer between anode active material and electrolyte phase are derived. They are introduced starting with the deintercalation, going on with the transport through the SEI, and ending with the solvation of a lithium-ion and its desorption at the outer SEI interface.

In the first step, intercalated lithium Li(s) is transferred to a vacant surface site V_{Li} at the sSEI-interface while leaving a vacancy and an electron in the active material, according to the following equation:



The reaction rate coefficients for the forward reaction $k_{f,s/\text{sSEI}}$

$$k_{f,s/\text{sSEI}} = k_{0,s/\text{sSEI}} \exp\left(-\frac{E_{a,s/\text{sSEI}}}{RT}\right) \exp\left(\frac{\alpha\Delta\phi_{\text{sSEI}}F}{RT}\right) \quad (7)$$

and the backward reaction $k_{b,s/\text{sSEI}}$

$$k_{b,s/\text{sSEI}} = k_{0,s/\text{sSEI}} \exp\left(-\frac{E_{a,s/\text{sSEI}} - \Delta G_{s/\text{sSEI}}^0}{RT}\right) \exp\left(-\frac{(1-\alpha)\Delta\phi_{\text{sSEI}}F}{RT}\right) \quad (8)$$

are defined based on the Arrhenius equation, with the reaction rate constant $k_{0,s/\text{sSEI}}$, the standard Gibbs free energy $\Delta G_{s/\text{sSEI}}^0$, the activation energy $E_{a,s/\text{sSEI}}$, and the electrochemical potential at the interface between active material and SEI $\Delta\phi_{\text{sSEI}}$. For this reaction, the standard Gibbs free energy is defined as

$$\Delta G_{s/\text{sSEI}}^0 = \mu_{\text{Li}(\text{sSEI})}^0 + \mu_{V_{\text{Li}}(s)}^0 + \mu_{e^-}^0 - \mu_{\text{Li}(s)}^0 - \mu_{V_{\text{Li}}(\text{sSEI})}^0 \quad (9)$$

with the standard chemical potentials μ^0 listed in Table SI-3. Finally, the overall volumetric reaction rate $r_{s/\text{sSEI}}$ at the sSEI-interface is described as an elementary charge-transfer reaction.^[50] It depends on the forward and backward reaction rate constants k_f and k_b , the ratio between the number of occupied and total surface sites, i.e., the surface coverages θ_{sSEI} and $\theta_{\text{SEI}/e}$, the surface site density Γ_{SEI} , the activity of lithium-ions a in their respective states, and the specific surface area a_s :

$$r_{s/\text{sSEI}} = a_s \Gamma_{\text{SEI}} \left[a_{\text{Li}(s)} (1 - \theta_{\text{sSEI}}) k_{f,s/\text{sSEI}} - a_{V_{\text{Li}}(s)} \theta_{\text{sSEI}} k_{b,s/\text{sSEI}} \right]. \quad (10)$$

The required activities of lithium in the active material are obtained with a Redlich-Kister approach.^[50] In this work, the surface site density is the same for both SEI interfaces. As a result, both the de-/intercalation reaction and the de-/adsorption process are influenced by this parameter. Future studies

may use different values for the inner and the outer SEI interface as a function of its local composition and surface structure or rather roughness.

The volumetric reaction rate of the generic reaction i can be transformed into the corresponding volumetric lithium-ion current with

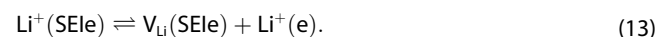
$$j_i^{\text{Li}} = r_i F. \quad (11)$$

The lithium-ion transport $\dot{n}_{\text{sSEI/SEIe}}$ between the inner (sSEI) and outer (SEIe) interface of the SEI is driven by potential and concentration gradients, i.e., migration and diffusion, respectively.^[19,54] For the sake of simplicity, the curvature of the SEI is neglected due to its small thickness compared to the underlying particle radius.^[55] This allows to use the same specific surface area a_s for the inner and outer interface of the SEI. The earlier discussed transference number for lithium-ions in the SEI $t_{\text{p,SEI}}$ accounts for deviations from a single ion conductor. This results into:

$$\dot{n}_{\text{sSEI/SEIe}} = -D_{\text{Li,SEI}} \Gamma_{\text{SEI}} a_s^2 \frac{\theta_{\text{SEIe}} - \theta_{\text{sSEI}}}{d_{\text{SEI}}} + \frac{t_{\text{p,SEI}} j^{\text{tot}}}{F}. \quad (12)$$

To reduce the computational burden of the SEI implementation, we went without a spatial discretization. This is valid if transport through the SEI is fast and gradients within this thin surface film are small.

The final process step, i.e., the solvation and desorption of lithium-ions at the SEIe-interface, is defined analogously to the deintercalation reaction at the sSEI-interface in Equations (6)–(10). During the desorption process, a lithium-ion from the SEIe-interface is transferred into the electrolyte phase while leaving a vacant surface site according to



The forward reaction rate is given by

$$k_{\text{f,SEIe/e}} = k_{0,\text{SEIe/e}} \exp\left(-\frac{E_{\text{a,SEIe/e}}}{RT}\right) \exp\left(\frac{\alpha \Delta \phi_{\text{SEIe}} F}{RT}\right) \quad (14)$$

and the backward reaction rate by

$$k_{\text{b,SEIe/e}} = k_{0,\text{SEIe/e}} \exp\left(-\frac{E_{\text{a,SEIe/e}} - \Delta G_{\text{SEIe/e}}^0}{RT}\right) \exp\left(-\frac{(1-\alpha) \Delta \phi_{\text{SEIe}} F}{RT}\right). \quad (15)$$

The standard Gibbs free energy is obtained via

$$\Delta G_{\text{SEIe/e}}^0 = \mu_{\text{V}_{\text{Li}}(\text{SEIe})}^0 + \mu_{\text{Li}(\text{e})}^0 - \mu_{\text{Li}(\text{SEIe})}^0. \quad (16)$$

The volumetric de-/adsorption rate of lithium-ions is defined based on power-law kinetics:^[18]

$$r_{\text{SEIe/e}} = a_s \Gamma_{\text{SEI}} [\theta_{\text{SEIe}} k_{\text{f,SEIe/e}} - a_{\text{Li}(\text{e})} (1 - \theta_{\text{SEIe}}) k_{\text{b,SEIe/e}}]. \quad (17)$$

Here, the activities for solvated lithium-ions in the electrolyte phase are obtained by normalization to a reference concentration (1 mol L⁻¹). The volumetric reaction rate can be converted into the corresponding volumetric current of lithium-ions with Equation (11).

The two following species balances describe the time dependence of the surface coverage at the interface between active material and SEI

$$a_s \Gamma_{\text{SEI}} \frac{\partial \theta_{\text{sSEI}}}{\partial t} = r_{\text{s/sSEI}} - \dot{n}_{\text{sSEI/SEIe}} \quad (18)$$

and at the interface between SEI and electrolyte phase

$$a_s \Gamma_{\text{SEI}} \frac{\partial \theta_{\text{SEIe}}}{\partial t} = \dot{n}_{\text{sSEI/SEIe}} - r_{\text{SEIe/e}} \quad (19)$$

with the corresponding interfacial reaction rates r_i and the transport through the SEI $\dot{n}_{\text{sSEI/SEIe}}$.

Finally, the charge balances for the electrochemical double-layers at the two SEI interfaces are introduced. It is assumed that the double-layer capacitance C^{DL} is constant with respect to potential and local lithium-ion concentration. The charge balances are given by

$$C_{\text{sSEI}}^{\text{DL}} \frac{\partial (\Delta \phi_{\text{sSEI}})}{\partial t} = \frac{j^{\text{tot}} - j_{\text{sSEI}}^{\text{Li}}}{a_s} \quad (20)$$

for the interface between the active material and the SEI and by

$$C_{\text{SEIe}}^{\text{DL}} \frac{\partial (\Delta \phi_{\text{SEIe}})}{\partial t} = \frac{j^{\text{tot}} - j_{\text{SEIe}}^{\text{Li}}}{a_s} \quad (21)$$

for the interface between the SEI and the electrolyte phase with the potentials at the double-layers $\Delta \phi_{\text{sSEI}}$ and $\Delta \phi_{\text{SEIe}}$, respectively.

Dynamics related to the current collectors

For an improved understanding of the SEI, it is important to differentiate between SEI-related and contact-related impedance contributions. Here, Gaberscek et al. shaped the commonly accepted impedance interpretation by investigating the origin of the high-frequency impedance arc in lithium-ion batteries beyond 1 kHz.^[56] They demonstrated clearly that this impedance contribution must be related to the contact between the electrode coating and the underlying metallic substrate, i.e., the current collector. For a meaningful physicochemical cell diagnosis, this should not be confused with the SEI and its reported characteristic frequency on the order of 250 Hz.^[57,58] For this reason and for the sake of completeness,

we include the anode and cathode contact resistances into our model.

The potentials at the double-layers at the anode ($\Delta\phi_{a,cc}$) and cathode ($\Delta\phi_{c,cc}$) current collector with the contact resistances $R_{a,cc}$ and $R_{c,cc}$ and the electric current I_{cell} are described with

$$C_{a,cc}^{DL} \frac{d(\Delta\phi_{a,cc})}{dt} = \left(\frac{I_{cell}(t)}{A_{cell}} - \frac{\Delta\phi_{a,cc}}{R_{a,cc}} \right) \quad (22)$$

and

$$C_{c,cc}^{DL} \frac{d(\Delta\phi_{c,cc})}{dt} = \left(-\frac{I_{cell}(t)}{A_{cell}} - \frac{\Delta\phi_{c,cc}}{R_{c,cc}} \right). \quad (23)$$

Both potentials at the double-layers are initialized at 0 V vs. Li/Li⁺. Eventually, the cell voltage can be calculated with

$$V_{cell} = \phi_c(I_{cell}) + \Delta\phi_{c,cc} - \phi_a(0) - \Delta\phi_{a,cc}. \quad (24)$$

Parameterization Strategy

As discussed before, the central purpose of the proposed SEI-extended P2D cell model is to enable a holistic cell diagnosis based on multiple measurement types for an in-depth understanding of the state of a lithium-ion battery and its changes during aging. Inevitably, this requires a sound parameterization strategy to avoid ambiguous and thus potentially misleading parameter estimates. For this reason, we employ a multi-step parameterization procedure to exploit individual parameter sensitivities that differ between the measurement techniques.

Figure 2 provides a condensed summary of the strategy for both the initial model parameterization and the later parameter update during cell aging.

The fundamental parameterization procedure is similar to our previous work.^[20] It highlighted that the commonly chosen approach for P2D cell model parameterization based on discharge curves cannot ensure good parameter identifiability. Although the experimental data may be represented accurately, a non-unique parameter set could lead to wrong conclusions with respect to limiting processes in the cell. To overcome this problem, a multi-step parameter estimation approach was used, using quasi-static discharge and dynamic EIS measurements in a three-electrode setup. In this work, we extend this parameterization strategy to account for the SEI. Table 1 summarizes the extracted parameters in each parameterization step from Figure 2. It specifies the already known parameters and the exploited measurement data for the parameter estimation, starting with low C-rate discharge for solid state concentrations (step I), moving on to high C-rate discharge for mass transport-related parameters (step II), and advancing to EIS data for kinetic parameters (step III). The corresponding objective functions are detailed in Section SI-1.3. The identifiability of the initial parameters and the identifiability of parameter changes due to aging are discussed in Section SI-1.4 and Section SI-1.5, respectively. Regarding the EIS analysis, only the medium frequencies between roughly 1 kHz and 5 Hz are used. In this range, the reaction kinetics and SEI-related processes take place, for which parameters are identified.^[41,57,58] Importantly, this frequency range is not accessible with a common discharge measurement, which underlines the impor-

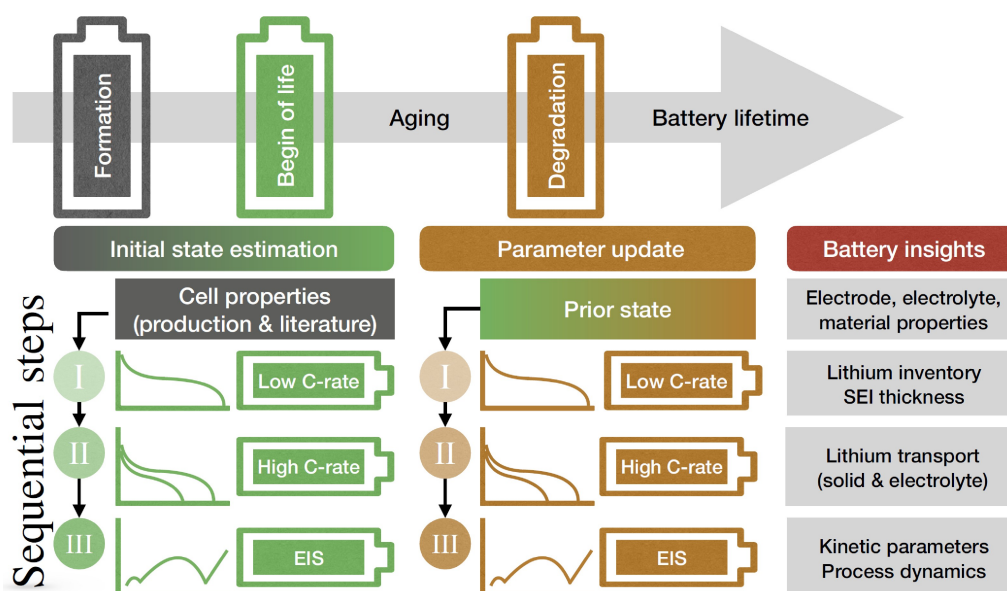


Figure 2. Schematic representation of the multi-step parameterization strategy for a model-based cell diagnosis of the SEI-extended P2D cell model with three-electrode measurements. Before any mathematical optimization is applied, well-known properties from electrode production like electrode thickness, porosity, and active material volume fraction are fixed. Further properties like the ionic conductivity of the utilized electrolyte system may be adopted from literature. Afterwards, three parameterization steps are executed sequentially for both the initial model parameterization after cell formation and the parameter update along cell cyclization. The parameter update of aging-sensitive parameters uses always the prior cell state. This can either be the initial state of a fresh cell after formation or an already updated parameter set from an earlier characterization snapshot during aging.

Table 1. Summary of the parameterization steps including the extracted parameters and the utilized (experimental) data sources for both the initial model parameterization and the update of aging-sensitive model parameters during cyclization. The experiments comprise anode and cathode half-cell data. The initial parameter values are summarized in Table SI-5.

Step	Data	Parameters (initial)	Parameters (update)
Cell properties	Electrode production	$d_{ar}, d_{sr}, d_{cr}, \varepsilon_{e,ar}, \varepsilon_{e,sr}, \varepsilon_{e,cr}, \varepsilon_{s,ar}, \varepsilon_{s,c}$	–
	Literature	Electrolyte properties	–
	OCP measurement	Activities, chemical potentials	–
	1 st formation cycle	d_{SEI}	–
I	C/10 discharge	$C_{a,0r}, C_{c,0r}, C_{a,maxr}, C_{c,max}$	$d_{SEI}, D_{s,c}$
II	1C, 2C discharge	$\tau_{ar}, \tau_{cr}, D_{s,ar}, D_{s,c}$	$\tau_{ar}, D_{s,c}$
III	EIS	$k_{0,s/SEI}, k_{0,SEI/e}, k_{0,cr}$	$I_{SEI}, k_{0,cr}$
		$C_{s,SEI}^{DL}, C_{SEI/e}^{DL}, C_c^{DL}$	$C_{s,SEI}^{DL}, C_{SEI/e}^{DL}, C_c^{DL}$
		$\sigma_{s,cr}, \sigma_{s,ar}, k_{SEI}^{DL}, R_{a,ccr}, R_{c,ccr}, C_{a,ccr}, C_{c,cc}$	k_{SEI}^{DL}

tance of a joint analysis of C-rate and EIS data for a holistic cell diagnosis.

Initial model parameterization

As the first step in any model parameterization, all already known or easily accessible parameters should be fixed. In this work, the electrode and separator thicknesses, the electrode porosity $\varepsilon_{e,r}$ and the active material volume fraction ε_s are known. Other parameters like the electrolyte conductivity and diffusivity may require tailored experiments, which are often already available in literature. For this work, the electrolyte properties are approximated with empirical polynomials for 1 M LiPF₆ in EC:EMC 3:7 (w:w) by Landesfeind et al.^[59] The anode and cathode open circuit potentials are described with a Redlich-Kister expansion. We extracted the corresponding Redlich-Kister coefficients from half-cell discharge data at a C-rate of C/50 after cell formation via nonlinear least-squares fitting (see Table SI-4).

Although not directly measurable, the initial SEI thickness after cell formation is calculated based on the initial capacity loss in the 1st formation cycle. In contrast to a mathematical optimization, this circumvents ambiguous results due to strong correlations with parameters like the SEI ionic conductivity. Model-based studies on SEI growth commonly use available image analysis data to estimate the SEI thickness or directly calculate it from the initial capacity loss during cell formation.^[17,18,23] We use the latter approach and estimate the SEI thickness based on the difference between charge and discharge capacity during the first formation cycle. Importantly, we attribute only part of the observed capacity loss during formation to irreversible SEI growth. The apparent capacity loss at high anode potentials is related to a reversible shift in the lithiation degree of the anode (see Section SI-1.2).

In general, a wide range of SEI growth reactions is possible within an LiPF₆ EC:EMC electrolyte system with a small amount of VC as a formation additive.^[11] Intertwined reaction pathways between these components and their intermediate reaction products further complicate the estimation of the exact SEI composition and its related lithium consumption.^[60] The formation data alone do not provide enough distinct features for a reasonable differentiation between different SEI growth

reactions and resulting SEI components. To enable a clear estimation of the SEI thickness, we attribute all SEI growth to the inorganic SEI component lithium carbonate like in our previous work,^[18] according to the following reaction:^[28]



The EC-related film thickness is calculated from the irreversible initial capacity loss (ICL) Q_{ICL} along with the molar volume of lithium carbonate $\tilde{V}_{Li_2CO_3}$:

$$d_{SEI} = \frac{Q_{ICL}}{2F} \tilde{V}_{Li_2CO_3} a_s^{-1}. \quad (26)$$

It is assumed that the SEI forms homogeneously throughout the anode. Relevant parameters for the thickness calculation are summarized in Table SI-5. Taking into account the SEI volume, the anode porosity is adjusted:

$$\varepsilon_{a,e}^{adjusted} = \varepsilon_{a,e}^{init} - d_{SEI} a_s. \quad (27)$$

Parameter update during aging

To determine, how the cell and the SEI changes during cyclization, aging-sensitive parameters are identified and updated after 50 and 100 aging cycles (see Table 1). The starting points for these mathematical parameter optimizations are the initial parameter set after formation and the updated parameter set after 50 aging cycles, respectively. Importantly, the parameters in this work were chosen based on their ability to capture the observed changes in the experiments. For other cells or different aging conditions, a reassessment of the selected aging-sensitive parameters is highly recommended.

In the first step, the SEI thickness d_{SEI} is updated with discharge data at a C-rate of C/10 to capture the observed loss of lithium inventory. Here, we attribute the full losses in capacity to SEI growth and not loss of active material. This assumption is supported by a differential voltage analysis of the experimental half-cell data, which does not show substantial changes in peak separation at low SOC on the anode side. In any other case, the parameterization would have to consider

the deactivation of (partially) lithiated active material. In the second step, the anode tortuosity and the cathode solid diffusion coefficient are adjusted based on 1C and 2C discharge data. These two parameters were found to be crucial to reproduce the observed changes in the respective half-cell voltages. In the final parameterization step, the EIS measurement is used to update the ionic conductivity of the SEI, its surface site density, and its two distinct double-layer capacitances. These parameters enable a lateral shift of the anode half-cell impedance, a direct manipulation of its kinetics via the surface site density, and a shift of its characteristic frequencies via the two capacitances. Here, it is assumed that changes in the kinetics are related to the available surface site density. However, a change in the reaction and adsorption rate constant, e.g., due to an altered interfacial composition would have the same effect on the cell behavior. Additional studies would be needed to decide on the physically more reasonable one. The SEI diffusion coefficient is not adjusted due to a lack of corresponding features in the experimental data. On the cathode side, the reaction rate constant and the double-layer capacitance are updated.

Experimental Section

The following experimental study is used for the model-based state estimation of a fresh cell directly after the formation process and along aging. Herein, the initial state estimation will help to assess the importance of individual SEI properties for both the cell performance at elevated C-rates and the impedance behavior. The subsequent analysis of cell behavior changes during aging via a parameter update will help to understand degradation or rather transformation processes within the cell.

The electrodes for the aging study in this work have an active material content of 93% for both the graphite anode and the NMC622 cathode. The porosity of these electrodes was estimated via mercury intrusion porosimetry. These and other parameters that were measured, known from production, or obtained from the initial model parameterization are summarized in Table SI-5.

For the electrochemical cell characterization, a commercial PAT-cell three-electrode setup by EL-Cell GmbH was used. The electrodes were punched to a diameter of 18 mm for the EL-Cell PAT-cell, afterwards weighed, and dried at 120 °C under high vacuum. Afterwards, they were transferred into an argon-filled glovebox for cell assembly. Here, the cathode was assembled as the lower electrode in the PAT-cell. To enable single electrode studies, a PP fiber/PE membrane separator by EL-Cell GmbH with an integrated lithium-metal reference electrode was used (ECC1-00-0210-V/X). The test cells were filled with 100 μ L electrolyte, which is composed of 1 M LiPF₆ conducting salt in a 3:7 (v:v) solvent mixture of ethylene carbonate (EC) and ethyl methyl carbonate (EMC) with 2 wt% vinylene carbonate (VC) as a formation additive. Cell formation and cyclization were done with an automated MACCOR series 4000 test system. The EIS measurements were performed with a Gamry Reference 3000 potentiostat/galvanostat. All measurements were performed at a temperature of 20 °C in an ESPEC SU-641 temperature chamber.

The cell formation procedure is performed with currents based on the theoretical capacity of the cathode. After formation, a capacity test at a C-rate of C/10 is applied to determine the practical capacity of the cell. This value is used to set the currents for the

respective C-rates during cell characterization and aging. The employed measurement routine with respect to cell formation, cell characterization, and cell aging is given in Table SI-6. In brief, after wetting and cell formation, a characterization procedure is applied, which comprises an EIS measurement and a C-rate test at various C-rates. Afterwards, a cell aging procedure is applied with 50 charge-discharge cycles between 2.9 V and 4.2 V. These two procedures are repeated for a total of three characterization snapshots along 100 aging cycles. Based on this measurement routine, two cells were assembled and tested. Due to similar results, one cell was selected for the model-based cell diagnosis in this work.

Results and Discussion

In this section, we will first evaluate how well the model can reproduce experimental discharge curves and impedance spectra, and what insight can be gained from the identified parameters. Subsequently, we follow the cell during its lifetime and identify the corresponding changes in model parameters.

Model-based insight into the initial battery state

In a first step, the capability of the model to reproduce experimental data is discussed. Afterwards, the identified SEI properties and their implications for cell performance are elaborated.

Figure 3 shows the initial battery state with experimental full-cell and half-cell discharge data as well as impedance spectra (solid lines) and compares them with the simulation results (dashed lines).

The full-cell discharge curves in Figure 3a show a good agreement between experiment and simulation for all investigated C-rates, comparable to other studies in the field.^[17,45] However, an underestimation of the cell voltage becomes visible in the upper voltage regime for C-rates at and above 1C. The half-cell discharge data in Figure 3c indicate that this observed underestimation of the cell voltage should mainly be attributed to the cathode side. Literature in this context suggests that this deviation may be related to the formation of a new phase within individual active material particles, which results into a sequential particle-by-particle charging and discharging mechanism, rather than a homogeneous concentration increase in all particles.^[61] Another study proposed an activity-based correction of the solid phase diffusion coefficient, which could improve the representation of experimental charge and discharge curves.^[51] It was also shown that mechanical-electrochemical volume changes of the active material can have a substantial effect on cell performance.^[62,63] Furthermore, the utilization of the median anode and cathode particle size rather than their respective particle size distributions likely also contributes to the observed deviations in the discharge behavior.^[44,64,65]

Figure 3b shows the experimental full-cell EIS measurement and the corresponding simulated impedance spectrum, which are in very good agreement as evident from the highlighted

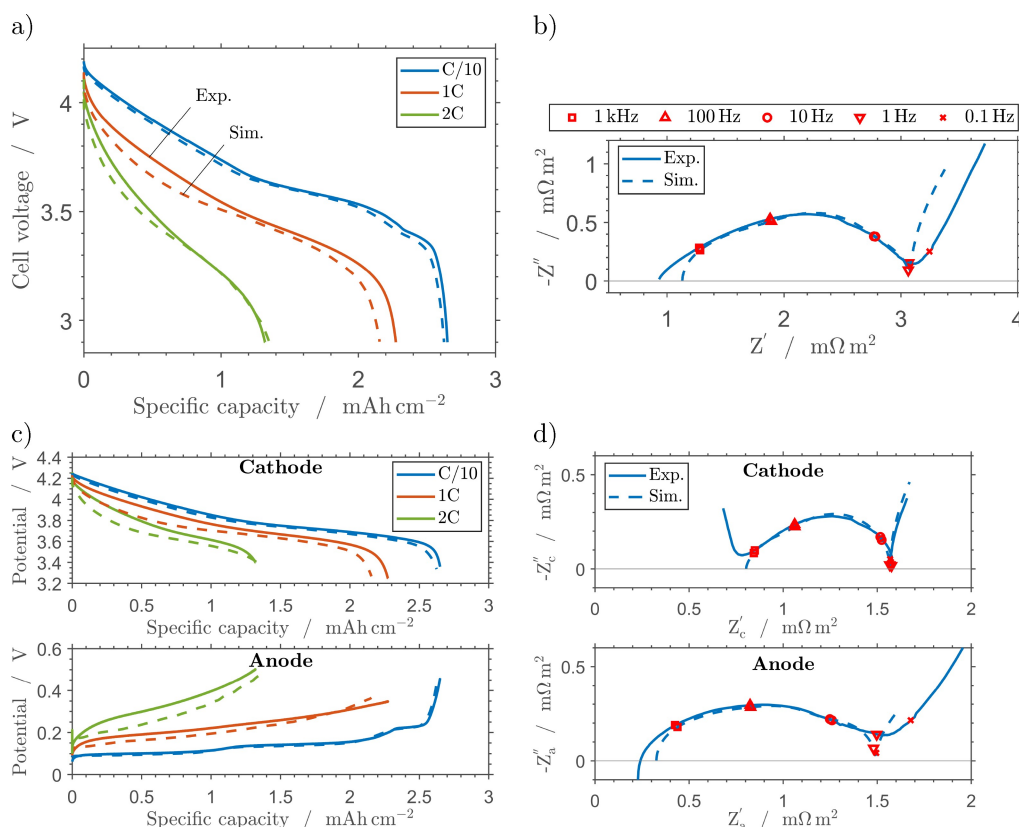


Figure 3. Simulations with the parameterized model (dashed line) and the experimental data (solid line) for a) full-cell and c) half-cell discharge curves at C/10, 1C, and 2C, and impedance spectra of b) full-cell and d) cathode and anode half-cell at 3.7 V. For a better comparison between experimental and simulated impedance spectra, five frequencies are highlighted with red markers: 1 kHz (□), 100 Hz (Δ), 10 Hz (○), 1 Hz (▽), and 0.1 Hz (×).

frequencies. At frequencies below 0.1 Hz, an almost linear slope can be observed, which is commonly attributed to diffusion in the active material. At higher frequencies between 1 Hz and 1 kHz, a non-ideal, i.e., depressed, semicircle can be seen. These frequencies are commonly attributed to charge transfer between active material and electrolyte as well as transport through the SEI.^[58] With our SEI understanding, a differentiation between SEI and charge transfer is not reasonable. We attribute these two dynamic processes to the SEI interfaces. As such, the SEI is inherently bound to the charge transfer, but the bulk SEI is not responsible for the observed dynamics.

For the interpretation of the half-cell impedance data in Figure 3d, it is important to be aware of limitations of the utilized three-electrode setup, which is known to introduce artefacts in the edge areas of the measured frequency range.^[66] Nonetheless, the half-cell responses at medium frequencies between 1 kHz and 5 Hz are still valuable. They were used for the parameterization in order to distinguish between anode and cathode processes. As a result, this frequency range is reproduced very well, which indicates a successful identification of process dynamics. The relatively poor representation of the lower frequency range in the full-cell and especially anode half-cell impedance suggests that the solid diffusion may not be captured accurately. The wide range of reported diffusion coefficients as a function of the intercalation degree also prevents the direct utilization of literature values, which

depend on graphite-type, electrode microstructure, and measurement technique.^[64]

The significantly depressed semicircle for the anode half-cell impedance in Figure 3d suggests the superposition of at least two dynamic processes. This supports the modeling of two independent anode processes (de-/intercalation, de-/adsorption). In contrast, the cathode half-cell impedance in Figure 3d shows an almost ideal semicircle, which suggests one characteristic process. Here, the almost linear impedance increase between 1 kHz and 100 Hz is related to the superposition of the dynamic response of multiple cathode particles. On the anode side, this theoretically also occurs but is not that well visible. Finally, above 1 kHz, the interface between electrode coating and current collector dominates the cell dynamics.^[25,56] However, a distinct feature for these dynamics, like observed in other studies, cannot be seen in our experiments.^[57] This renders the corresponding model parameters in our study less insightful.

Overall, the results show that the proposed model can adequately reproduce EIS measurements and discharge curves at different C-rates. Consequently, the obtained parameter values (see Table SI-5) are representative for this wide operational range and thus inherently more insightful than single-measurement estimates. In the following, the identified SEI parameters are discussed in detail.

The estimated SEI thickness is roughly 90 nm. This is within the range of other simulation studies on SEI growth. In our previous multiscale modeling study on SEI formation, we started without any SEI and advanced to a thickness of roughly 40 nm to 60 nm, depending on the formation current.^[36] Aging studies commonly start with SEI thicknesses below 50 nm and predict SEI growth during aging beyond 100 nm,^[23] 300 nm,^[67] or even 600 nm.^[17] Experimental studies commonly report values between roughly 3–100 nm.^[9,11,39] This divergence between experiments and aging-focused simulation studies also becomes visible in our parameter estimates along aging and most likely has a systematic origin.

Model-based studies commonly resort to an approximation of the specific surface area of the active material that is based on the assumption of perfectly spherical particles (see Table S1-2). The experimental study by Nowak et al. gives an idea of the validity of this simplification. They estimated the mass-specific surface area of different particle size distributions via the Brunauer-Emmett-Teller (BET) theory.^[68] Depending on the median particle size of the sample, the BET-based specific surface area is roughly three to nine times higher than the corresponding approximation with spherical particles. Such an underestimation would result into a proportional overestimation of the SEI thickness, which would explain the difference to experiments. For a quantitative parameter comparison between cells with the same electrode, this is not a problem as the initial microstructure is the same. With different electrodes, a comparison between SEI parameter estimates should be done with caution as long as realistic surface area measurements or model-based approximations are not available.

The estimated ionic conductivity of the SEI is roughly $830 \mu\text{S m}^{-1}$. Practical simulation studies that target the discharge characteristics along cell aging use ionic conductivities ranging from $100 \mu\text{S m}^{-1}$ to $10,000 \mu\text{S m}^{-1}$.^[17,67] Compared to studies that focus on transport properties of individual SEI components, these values are relatively high. For instance, Borodin et al. investigated lithium-ion transport in dilithium ethylene dicarbonate, Li_2EDC , which is a common organic SEI component for electrolytes containing ethylene carbonate.^[38] From both molecular dynamics simulations and experiments, they estimated an ionic conductivity on the order of $0.1 \mu\text{S m}^{-1}$. Shi et al. discussed defect thermodynamics in lithium carbonate, looking at its implications for charge transport in the SEI over a wide voltage range.^[40] For the anode side, their simulations provide a potential-dependent conductivity of roughly $0.01 - 1 \mu\text{S m}^{-1}$.

Obviously, the conductivity of these pure SEI components is significantly lower than the estimated ionic conductivity in our work. However, due to the multi-component nature of the SEI, the observed ohmic resistance will not be the result of just one component. Zhang et al. found that the poorly conductive LiF has a significant positive effect on the ionic conductivity of Li_2CO_3 .^[32] They suggested an improvement of this parameter by two orders of magnitude. Maibach et al. investigated potential gradients at the SEI interfaces using photoelectron spectroscopy.^[69] Ongoing SEI formation did not change their results significantly, suggesting a minimal potential gradient

over the SEI thickness, i.e., a high ionic conductivity. Considering both the underestimation of the active surface area, i.e., the overestimation of the ionic conductivity, and the synergistic effect between different SEI components, an estimated ionic conductivity of $830 \mu\text{S m}^{-1}$ points at a multi-component SEI in our cell.

Finally, the diffusion coefficient of lithium-ions in the SEI was adopted from density functional theory simulations for Li_2CO_3 by Shi et al.^[39] They suggested a diffusion coefficient of roughly $10^{-11} \text{ m}^2 \text{ s}^{-1}$ at 300 K and confirmed it with estimated SEI resistances from impedance measurements. To reproduce our experimental data, this value worked well and did not necessitate an adjustment. However, the following parameter study reveals that this may differ for cells with other SEI properties.

Impact of SEI parameters on EIS and C-rate performance

To gauge the importance of individual SEI properties for the overall cell behavior, we perform a sensitivity analysis for the SEI thickness, ionic conductivity, diffusion coefficient, and surface site density. In real batteries, a complex combination of multiple parameter effects is expected. For instance, not only the SEI thickness may change upon cell aging but also its composition and structure. Similarly, a different formation procedure or different electrolyte additives would be expected to alter all SEI-related properties. To understand their individual contributions to the cell behavior, we analyze the four mentioned SEI parameters separately. This will also help to perform a rough assignment of the most probable parameter changes in experimental data without a detailed model-based analysis.

Figure 4 and Figure 5 show the effect of these parameters on the full-cell discharge and impedance behavior, respectively. The medium values correspond to the estimated initial battery state from the previous section. The SEI thickness was found to have a relatively high sensitivity. Thus, this parameter is varied by roughly $\pm 50 \text{ nm}$, whereas the other ones are varied more widely by a factor of 0.2 and 5.

The SEI thickness in Figure 4a shows a clear effect on all investigated C-rates from C/10 to 2C. Primarily, this is due to the direct relation between SEI growth and lithium loss. In addition, SEI growth impacts mass transport in the electrolyte phase via a reduced electrode porosity, which leads to an increased tortuosity according to the Bruggeman relation. For the two SEI thickness variations of 50 nm and 150 nm, this translates into a tortuosity decrease of roughly -5% and an increase of about $+9\%$ compared to the initial state, respectively. In contrast, a significant contribution of the SEI ionic conductivity and its diffusion coefficient can be ruled out. The corresponding discharge curves in Figure 4b and c are almost indistinguishable even at higher C-rates without the insets. Finally, the variations of the SEI surface site density in Figure 4d have an effect on the cell voltage especially at higher C-rates. The influence of this parameter on kinetics is visible right from the beginning of discharge. As such, it can be easily

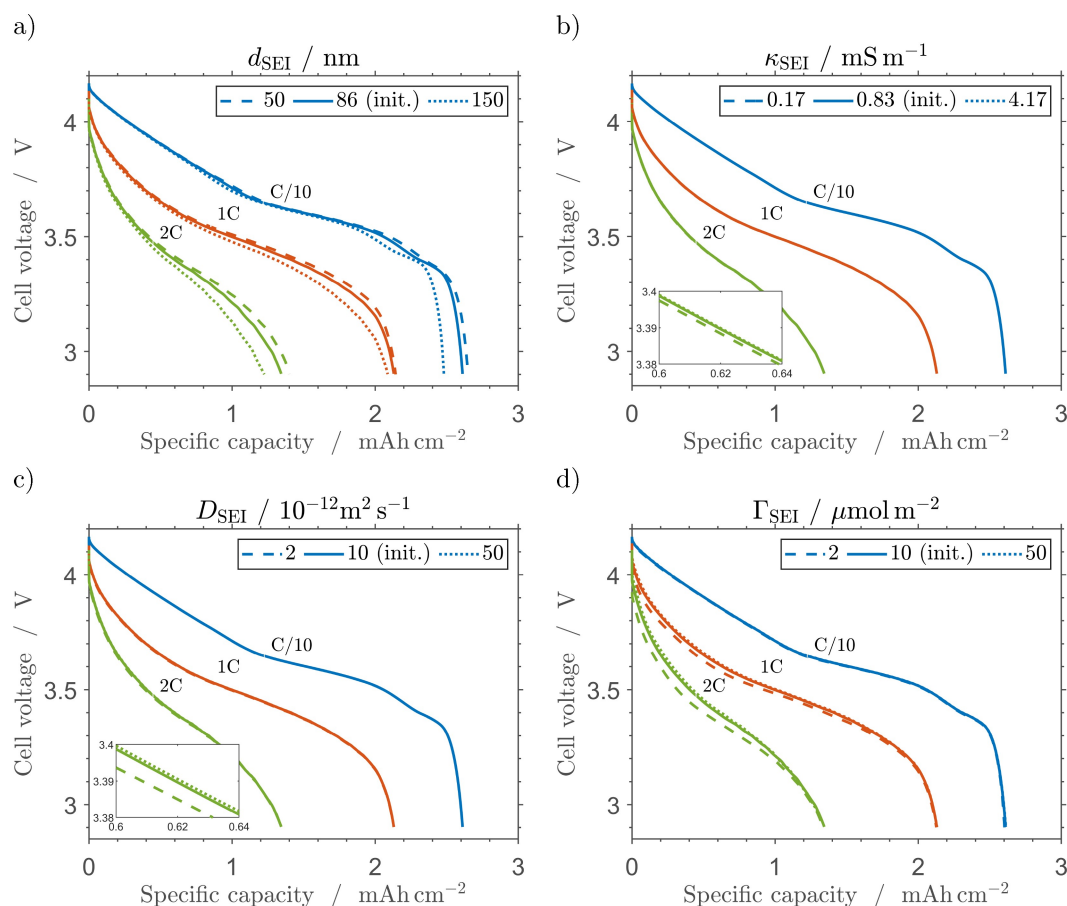


Figure 4. Simulated discharge curves for C/10, 1C, and 2C for a variation of a) SEI thickness, b) ionic conductivity of the SEI, c) diffusion coefficient of lithium in the SEI, and d) SEI surface site density. The simulation of the initial battery state is shown as a reference in each plot (solid line). The simulations are performed with the same conditions as the experiments.

differentiated from the SEI thickness, which has a more pronounced effect toward the end of discharge. This delayed effect is related to mass transport limitations in the electrolyte phase and a reduced lithium inventory.

In Figure 5a the influence of the SEI thickness on the impedance response is analyzed. It can be seen that it mainly yields a higher impedance at the Z' -axis intercept at high frequencies along with a parallel shift of the whole spectrum. This is related to its effect on the ohmic resistance of the surface film, and thus the overall ohmic resistance of the cell. For comparison, equivalent circuit models commonly differentiate between the dynamics of the SEI, the dynamics of the anode charge transfer, and the ohmic resistance of the cell.^[25,41,70] In these studies, the SEI resistance likely refers to its ohmic properties. However, it could also refer to a reaction resistance at its interface. In our model, the distinction is clear: The bulk SEI does not have a capacitance. As such, its ionic conductivity does not significantly alter interfacial kinetics for reasonably chosen values.

Figure 5b shows the effect of the SEI ionic conductivity. Here, a lower conductivity mostly affects the Z' -axis intercept at high frequencies without a proportional shift of the low-frequency impedance toward higher resistances. This behavior likely originates from the implementation of the SEI as a

combination of two interfacial processes and one transport process across the SEI. Its conductivity affects the potentials in both the active material and the electrolyte phase (see Equation 4). As a result, an adjustment of this parameter inherently alters the conditions for both the intercalation reaction and the adsorption process. Common equivalent circuit models do not consider this kind of overarching effect of the SEI on adjacent processes. As discussed before, they rather separate charge transfer and SEI into two separate resistor-capacitor elements.

In Figure 5c, the variation of the SEI diffusion coefficient reveals a possible additional semicircle around a frequency of 1 Hz upon a decrease of this parameter. At the same time, this shifts the roughly 45°-inclined impedance response below 0.1 Hz to higher ohmic values. When the diffusion coefficient is increased, the time constant of the diffusion process decreases. The additional semicircle disappears. In this case, the shape of the impedance spectrum between roughly 100 Hz and 10 Hz changes and becomes less depressed, i.e., it approaches the form of an ideal semicircle. This suggests that a higher diffusion coefficient causes an overlap with kinetics. In this work, this parameter was not optimized based on our experimental data but rather adopted from literature. If experiments show an

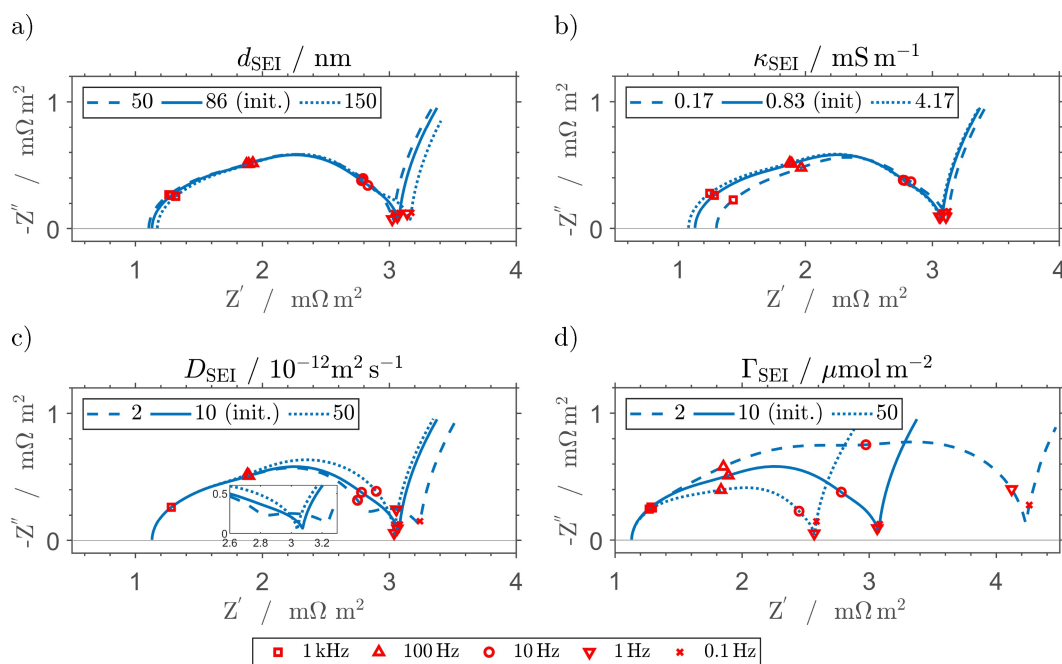


Figure 5. Simulated full-cell impedance spectra at 3.7 V with the parameterized model for a variation of a) SEI thickness, b) ionic conductivity of the SEI, c) diffusion coefficient of lithium in the SEI, and d) SEI surface site density. The simulation of the initial battery state is shown as a reference in each plot (solid line). The simulations are performed with the same conditions as the experiments. For a better understanding of the underlying process changes, five frequencies are highlighted with red markers: 1 kHz (\square), 100 Hz (Δ), 10 Hz (\circ), 1 Hz (∇), and 0.1 Hz (\times).

additional feature around 1 Hz,^[18] an update of this parameter may become necessary.

Finally, Figure 5d shows the variation of the SEI surface site density for occupation by lithium-ions. Here, a lower value creates a larger but still significantly depressed semicircle, which is composed of three visually distinguishable processes, namely cathode insertion, anode deintercalation at the solid-SEI interface, and desorption at the SEI-electrolyte interface. Here, especially the dynamic at the outer SEI interface, i.e., the de-/adsorption process, contributes to the impedance increase. A higher surface site density, i.e., more places for occupation by lithium-ions, substantially decreases the impedance response. This behavior is well expected as the surface site density has a direct effect on the interfacial reaction and process kinetics (see Equation 10, 17). As mentioned earlier though, a change of the surface site density without a change in SEI composition, i.e., ionic conductivity, is not expected for real batteries.

In summary, the performed parameter study highlights that the ionic conductivity and the diffusion coefficient of the SEI have an almost negligible effect on the discharge behavior but a notable effect in the impedance spectra. In contrast, the SEI thickness and the surface site density can influence the complete cell behavior. Nonetheless, the interfacial properties of the SEI remain much more sensitive in the EIS simulations. This indicates that the interfacial and bulk properties of the SEI are less relevant for the optimization of a cell's discharge performance. However, these parameters may be the key for a better understanding of cell aging.

The results further illustrate the importance of a multi-step parameter estimation similar to previous works.^[20,71] For instance, the SEI thickness in our model is directly related to the loss of lithium inventory. The analysis of a discharge curve at a low C-rate enables a parameter estimation without significant parameter interactions due to negligible kinetic and transport limitations. If the SEI thickness was instead extracted from an EIS measurement, the experimental data could also be reproduced by adjusting the SEI ionic conductivity (see Figure 5). For this reason, the earlier introduced multi-step parameterization strategy is so important (see Figure 2, Table 1).

Impact of aging on cell state and SEI properties

The results from the model-based cell diagnosis along cell aging provide in-depth insights into the underlying reasons for cell behavior changes. A better understanding of these degradation mechanisms lays the foundation for better aging predictions. Furthermore, it facilitates cell design improvements to mitigate cell degradation in the first place. In the following, the experimental data for aging cycle 50 and 100 are analyzed. Subsequently, the updated model parameters are discussed with respect to their contribution to the observed cell behavior changes.

Figure 6a and b show the experimental and the simulated discharge curves for cycle 50 and 100. The performance at cycle 0 is shown for comparison (black lines). It can be seen that the capacity at C/10 decreases significantly during the first 50 aging

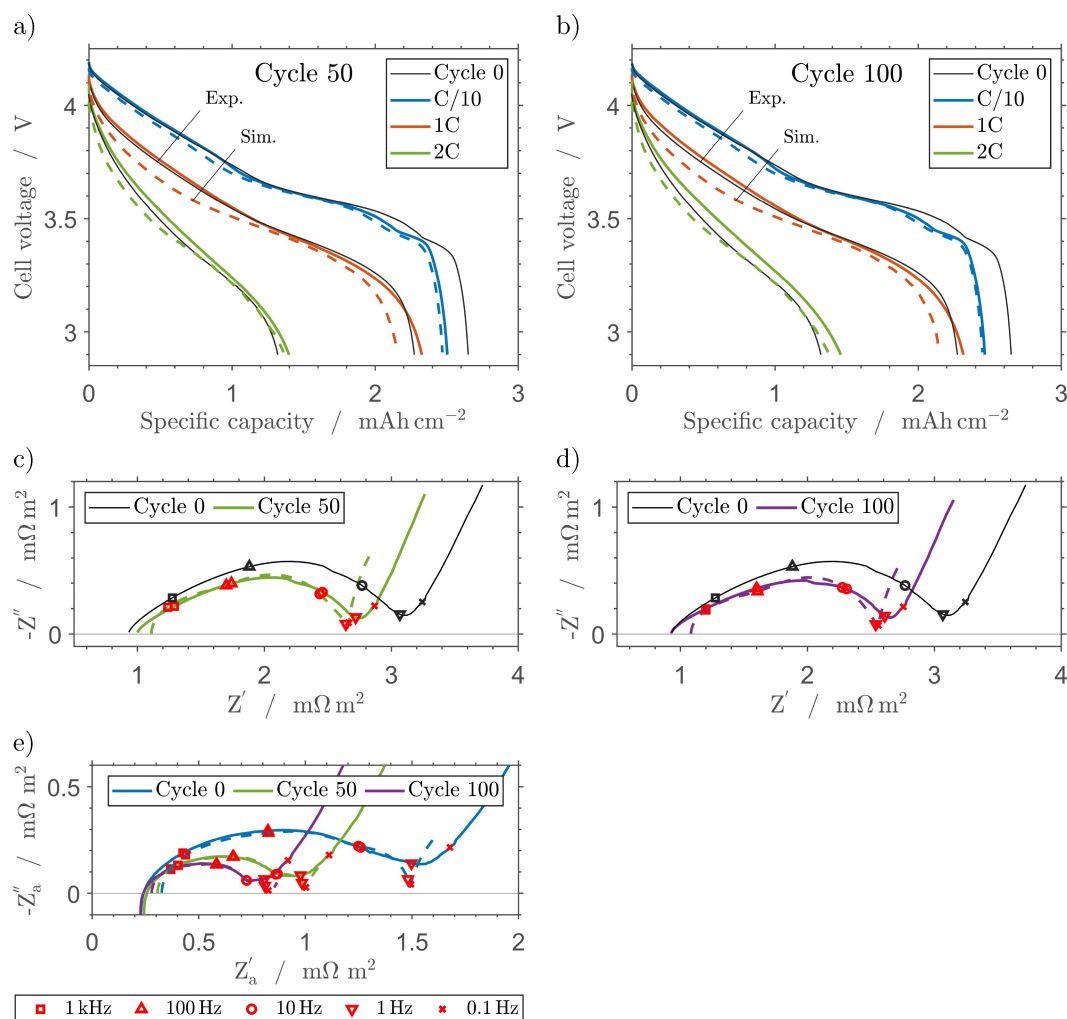


Figure 6. Comparison of experimental discharge curves (solid lines) and simulations after the model-based cell diagnosis (dashed lines) for a) cycle 50 and b) cycle 100. Experimental data for cycle 0 is shown for comparison (solid black lines). Experimental impedance spectra at 3.7 V (solid line) are compared with corresponding simulations (dashed line) for c) cycle 50 and d) cycle 100. The experimental data for cycle 0 is again shown with a solid black line for comparison. e) Experimental and simulated anode half-cell impedance spectra for cycle 0, 50, and 100. Five frequencies are highlighted with red markers: 1 kHz (□), 100 Hz (Δ), 10 Hz (○), 1 Hz (▽), and 0.1 Hz (×).

cycles (−5.5%). The additional capacity loss during the subsequent 50 cycles is relatively small (−1.5%). In contrast, the performance at 2C improves over the course of the first 50 aging cycles (+5.8%) and even further during the subsequent 50 cycles (+4.7%).

The simulations capture the capacity decline at C/10 very well. The performance improvement at 2C is reproduced qualitatively by the simulations although the total improvement is moderately underestimated. In our model, the capacity loss at low C-rates is attributed to SEI growth (see Figure 4a). However, a pure thickness increase would result in lower capacities also at higher C-rates, which is not observed in the measurements. Instead, the parameter update (over-) compensates this anticipated performance decline. Regarding kinetics, the surface site density may have increased, though the effect on the discharge capacity was small in Figure 4d. The remainder of the performance improvement may be attributed to reduced transport limitations in both anode and cathode.

For a deeper understanding of the observed performance improvement, the impedance behavior changes are analyzed.

The comparison between the full-cell EIS measurements and simulations at aging cycle 50 and 100 are shown in Figure 6c and d, respectively. The experimental impedance spectrum directly after cell formation, i.e., aging cycle 0, is provided for comparison in both figures. It can be seen that the full-cell impedance decreases substantially within the first 50 aging cycles. Between cycle 50 and 100, the spectrum changes less significantly. Here, only a small additional decrease of the semicircle between roughly 1 kHz and 1 Hz can be observed, which points at kinetic improvements.

To identify the origin of the impedance decline, Figure 6e shows the anode half-cell impedance along aging. It reveals that the anode impedance between cycle 0 and 50 decreases more rapidly than the full-cell impedance, which implies a simultaneous rise of the cathode impedance. On the anode side, the significant impedance reduction upon cycling points at substantial improvements in cell kinetics. A similarly strong

decline of the anode half-cell impedance was observed in literature in the context of manganese poisoning of the SEI, which alters its interfacial properties.^[14] However, this work uses NMC622 rather than lithium-manganese-oxide as the cathode active material so that manganese dissolution on the cathode side should be less of an issue.^[72] Another explanation may be a kinetically favorable evolution of its interfacial composition and structure due to the decomposition of less stable SEI components. Regarding the slight increase of the cathode impedance during cycling, both the formation of a surface layer and a surface reconstruction of the active material seem reasonable.^[52,73] A precise identification of the actual degradation mechanism would require additional experiments like X-ray diffraction to elucidate changes in the active material crystal structure. Although out of scope of this work, this kind of targeted experiments cannot (yet) be substituted with a model-based cell diagnosis based on simple measurements. For a truly knowledge-based optimization of a cell's aging

characteristics, this additional level of insights into the cell would be beneficial.

In the following, the evolution of the model parameters along cell aging is discussed. In Figure 7, the parameter estimates are given both as absolute parameter values and relative parameter changes with respect to the initial battery state, i.e., cycle 0.

As already expected based on the experimental discharge data, there is ongoing but significantly decelerating SEI growth. This explains the substantial capacity decline during the first 50 aging cycles, followed by a marginal additional decline during the subsequent 50 cycles. This trend is in good agreement with research on SEI-related capacity fade.^[23,74]

The ionic SEI conductivity shows first a moderate increase after 50 cycles and rises even more significantly up to cycle 100. On the chemical level, the identified conductivity increase of the SEI may be related to i) a change in the SEI composition due to the decomposition of less stable and also less

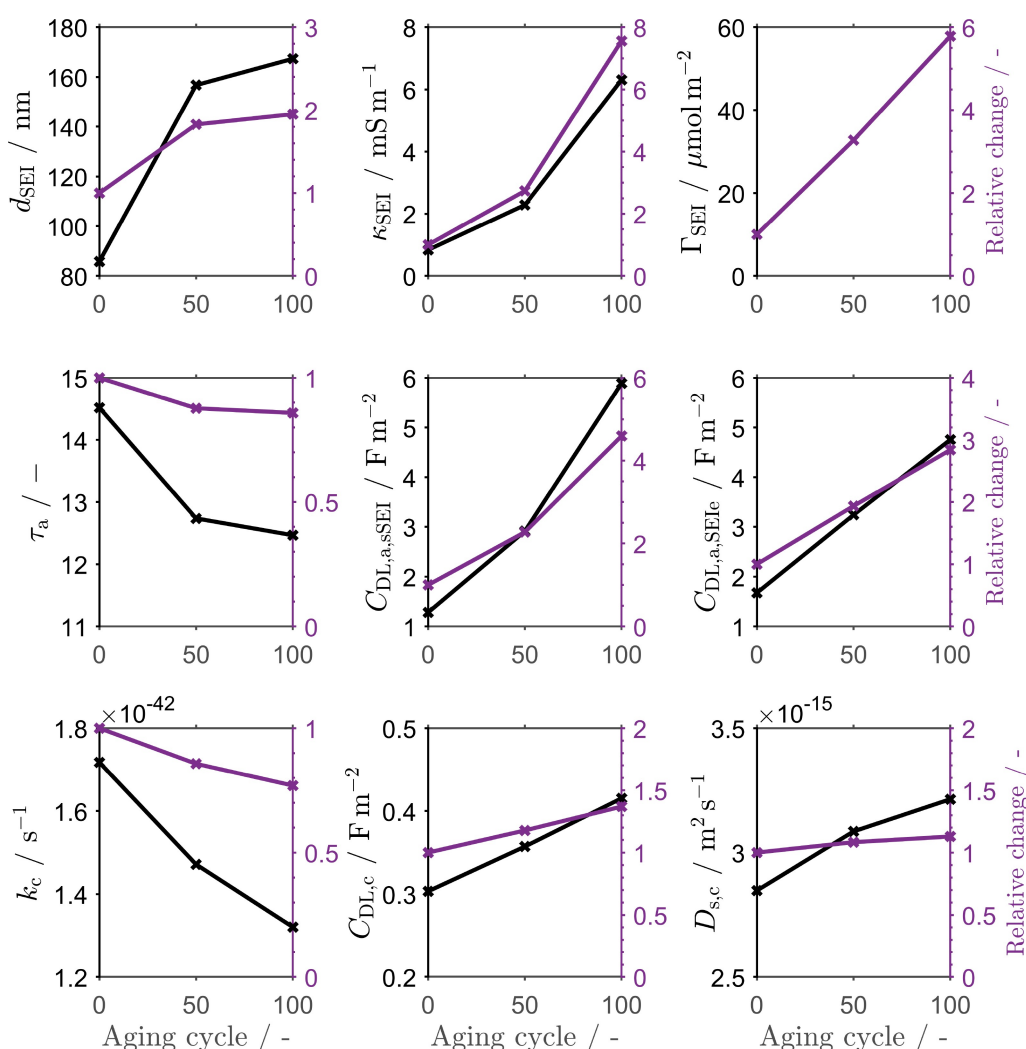


Figure 7. Parameter estimates from the model-based cell diagnosis along the first 100 aging cycles after cell formation. The first row shows the evolution of the SEI thickness, its ionic conductivity, and its surface site density. The second row shows the anode tortuosity as well as the active material-side and the electrolyte-side double-layer capacitance of the SEI. The third row shows the cathode reaction rate constant, its double-layer capacitance, and the cathode solid diffusion coefficient. Absolute parameter values are indicated by black markers; relative parameter changes are shown with purple markers.

conductive components like Li_2EDC ^[38] or ii) a performance-enhancing doping of the SEI with synergistic components like LiF .^[32]

The surface site density increases almost linearly during aging. This improves kinetics and yields a decline in anode impedance as well as a performance improvement during discharge. A possible explanation for a higher surface site density is an increased surface roughness: Due to the multi-component nature of the SEI, it is likely that a partial decomposition of less stable components could alter its structure and create a rougher surface with more available surface sites. Furthermore, the mechanical stress on the SEI due to the volume expansion of the anode active material during cycling can induce cracks in the surface film.^[12,75] Although these cracks would heal by a rapid formation of new SEI, this would alter its surface structure. Alternatively, the observed improvement of kinetics could also relate to a change in interfacial species that may facilitate, e.g., electrolyte stripping.^[76] As such, the increased surface site density may refer to either a larger active surface area, faster kinetics at the same surface sites, or most likely a combination of both. Again, additional experiments like depth profiling,^[77] spatial resistivity mapping,^[78] or imaging of the SEI^[11,79,80] could help to identify the underlying reason for this parameter change by providing a better understanding of SEI structure and composition.

The anode tortuosity was found to decrease by 14.1% during aging, suggesting improved transport in the electrolyte phase. Further, the tortuosity change depends on cell age: there is a substantial tortuosity decline up to cycle 50 (−12.3%) and an additional decline up to cycle 100 (−1.8%). The SEI-related reduction of the anode pore space compensates only little of this mass transport improvement. There are multiple possible explanations for the tortuosity decrease, i.e., the improvement of the effective transport properties in the anode electrolyte phase: This change may originate from i) gaseous species^[81] that are trapped within the cell and that escape over time, ii) a partial decomposition of less stable SEI components,^[11] or iii) a change in the overall transport properties of the electrolyte as a result of dissolved reaction products from the SEI formation. The first option could be investigated by using a different cell format, which allows for degassing after cell formation. Changes in the microstructural properties of the anode could be investigated via mercury intrusion porosimetry^[68] or FIB/SEM tomography,^[82] which may help to detect a shift in the incremental pore volume distribution. However, maintaining the formed SEI structure during the sample preparation would be challenging. Furthermore, the swelling of the binder upon contact with liquid electrolyte could not be considered. Finally, the cell formation process itself may change the effective transport properties in the electrolyte phase. In this context, Ushirogata et al. proposed a near-shore aggregation mechanism based on DFT simulations to explain SEI formation.^[83] Within this mechanism, reaction products do not directly become part of a solid surface film. Instead, they desorb, diffuse into the electrolyte phase, and form aggregates. These aggregates finally coalesce and complete the SEI formation upon contact with the electrode.

However, some reaction products may still be present in the bulk electrolyte phase after the cell formation process is officially finished. Whereas some reaction products may only remain temporarily in the electrolyte phase until further reaction or aggregation,^[84,85] others like lithium butylene dicarbonate may not precipitate on the electrode surface at all due to their high solubility.^[86] As a result, a long-term effect of these species on lithium-ion transport within the electrolyte phase may be expected. In the end, a comprehensive experimental analysis of the electrolyte after cell formation would be necessary to identify the cause for changes in the mass transport in the electrolyte, and thus in the adjusted parameter τ_a .

The double-layer capacitance at the interface between SEI and electrolyte increases by a factor of about three during aging. Evaluated on its own, this would shift the time constant of the adsorption process toward higher values, according to $\tau = R \cdot C$. Overall, the experimental data show a slight shift of the 10 Hz frequency point toward the left side, i.e., higher frequencies. However, the surface site density increases even more significantly during aging, i.e., the process resistance decreases (see Figure 6e). This insight is surprising, as capacitance is the product of surface area and specific capacitance. As a result, a proportional change of surface site density and capacitance would have been expected. It can be concluded that the specific capacitance and with it the physical nature of the double-layer, i.e., the permittivity of the SEI, must have changed.

Similar to the outer SEI interface, the double-layer capacitance at the inner interface between anode active material and SEI also increases along aging. However, it changes by a factor of about four instead of three, indicating a different SEI composition at its two interfaces. This is in good agreement with the experimentally observed two-layer structure of the SEI.^[77]

Finally, the cathode-related parameters are discussed. As a reminder, we simplified the cathode-side processes at the active material particles to one effective process, which is similar to common ECMs.^[25,87] A brief look at the anode and cathode half-cell impedance in Figure 3d underlines that this is a valid assumption for our cell. The cathode impedance between 0.1 Hz and 100 Hz resembles an almost perfect semicircle, corresponding to one dynamic process. The more linear stretch at higher frequencies originates from the spatial distribution of particle relaxations in the electrode and partially from an overlap with the contact resistance. Nonetheless, the model could be easily extended by a cathode surface film. This would be necessary, e.g., if the impedance had more similarity with a depressed semicircle, which would suggest the superposition of more than one dynamic process.

As expected based on the experimental impedance data, the reaction kinetics on the cathode side deteriorate with cyclization. Although the degradation decelerates slightly from cycle 50 (−14.3%) to cycle 100 (−8.8%), the trend suggests ongoing aging similar to our previous work.^[18]

The double-layer capacitance on the cathode side increases by 17.7% from cycle 0 to cycle 50 and an additional 19.2% up

to cycle 100. This indicates changes in the nature of the interface between active material and electrolyte. In addition, the often discussed mechanical degradation of the active material particles^[52,72,88] may also contribute to the increase of the capacitance via an increase of active surface area.

The solid diffusion coefficient in the cathode active material was found to affect mainly the end of discharge. It increased by 8.3% until cycle 50 and by an additional 4.6% up to cycle 100. A possible reason for this could be again the formation of cracks in the active material, shortening solid diffusion pathways. However, the electron transport distance would increase at the same time, rendering the overall impact of microcracks on cell performance unclear.^[89] It was also reported that a coating with Al₂O₃ during active material production improves both charge transfer and apparent solid diffusion.^[90] Although this specific surface species cannot explain our estimated diffusion improvement, it illustrates the possible impact of any surface film on the apparent diffusion coefficient. To identify the actual reason behind this parameter change, an experimental examination of the particles' structure and surface composition would be necessary.

Conclusion

In this paper, we show the first physicochemical lithium-ion battery and SEI model, which not only reproduces EIS data and discharge curves, but that can also be used for a detailed analysis of the battery state. Within this model, our understanding of the SEI comprises two interfacial processes, which are connected by the bulk SEI via migration and diffusion. This detailed modeling allows not only to look at the state and limiting processes within a cell, but it also allows to trace back changes in cell behavior to distinct cell and SEI properties. Our analysis highlights that SEI growth does not inevitably lead to an impedance rise. In most equivalent circuit models, the SEI resistance represents one dynamic process, which i) would trigger an impedance increase upon SEI growth or ii) lump together the effect of SEI thickness, conductivity, and interfacial process kinetics. In either case, this prevents a precise localization of performance limitations and degradation processes. Our model allows for a reasonable explanation of a shrinking anode impedance despite ongoing SEI growth by considering changes in its interfacial processes.

During the initial battery state estimation, we found that the SEI thickness in our and other simulation studies are systematically overestimated compared to experiments. In battery models, the linearly related specific surface area is commonly calculated for a representative spherical particle. Measurements of this parameter from other studies reveal much larger values, which originate from both non-uniform particle size distributions and non-spherical particle shapes. To make SEI parameter values comparable between different electrode designs, a measurement or a reliable approximation of the specific surface area is recommended.

The model-based aging analysis offered a perspective on the evolution of SEI properties after formation. It could be

shown that SEI growth with its consumption of cyclable lithium and a change in electrode porosity has a significant effect on a cell's discharge behavior. The ionic conductivity of the SEI was found to be relatively high compared to pure SEI components, suggesting significant synergistic effects. This also means that a fine-tuning of the bulk SEI composition in our cell could not offer a meaningful improvement in discharge performance. In contrast, the interfacial characteristic of the SEI, i.e., its surface site density, significantly influences the impedance response, but it also has a distinct effect on the overpotential during discharge. Its substantial increase along aging due to a drastic anode impedance decline suggests fundamental changes in the interfacial composition and structure of the SEI. Such significant changes could serve as a predictor for cell aging or even enable a better understanding of the cell formation process.

In the end, the experiments in this work were designed to demonstrate the in-depth insights into the cell state with the proposed modeling and diagnostics concept. Future studies may consider to extend the model-based cell diagnosis to large-format cells without reference electrodes. Here, additional measurements like the nonlinear frequency response analysis^[91] or model-defined experiments may help to distinguish between anode- and cathode-related processes based on full-cell data. This would provide access to detailed cell diagnostics for large-scale applications like quality gates in battery production or data mining on battery usage data.

Supporting Information

The abbreviations and symbols are defined in the Supporting Information.

Acknowledgements

This work was supported by the German Federal Ministry for Economic Affairs and Energy through funding of the project "DaLion 4.0 - Data Mining as Basis for cyber-physical Systems in Production of Lithium-ion Battery Cells" (03ETE017A). The authors would also like to thank the DaLion 4.0 team at the TU Braunschweig and especially Alexander Schoo and Marcel Dittmer of the Institute for Particle Technology (iPAT) for the production and porosity analysis of the electrodes within the Battery LabFactory Braunschweig (BLB), Louisa Hoffmann of the Institute for High Voltage Technology and Electrical Power Systems (elenia) and Dr. Tom Patrick Heins of the Institute of Environmental and Sustainable Chemistry (IÖNC) for fruitful discussions on electrochemical cell characterization procedures, and Lars Bläubaum from Karlsruhe Institute of Technology at the Institute for Applied Materials - Electrochemical Technologies (IAM-ET) for valuable advice regarding hands-on and in-depth electrochemical cell characterization. Open Access funding enabled and organized by Projekt DEAL.

Conflict of Interest

The authors declare no conflict of interest.

Data Availability Statement

The data that support the findings of this study are available from the corresponding author upon reasonable request.

Keywords: cyclization · impedance · interfaces · P2D model · three-electrode setup

- [1] Y. Li, M. Abdel-Monem, R. Gopalakrishnan, M. Bercibar, E. Nanini-Maury, N. Omar, P. van den Bossche, J. Van Mierlo, *J. Power Sources* **2018**, *373*, 40–53.
- [2] C. Pastor-Fernández, K. Uddin, G. H. Chouchelamane, W. D. Widanage, J. Marco, *J. Power Sources* **2017**, *360*, 301–318.
- [3] S. Golmon, K. Maute, M. L. Dunn, *Int. J. Numer. Methods Eng.* **2012**, *92*, 475–494.
- [4] O. Schmidt, M. Thomitzek, F. Röder, S. Thiede, C. Herrmann, U. Krewer, *J. Electrochem. Soc.* **2020**, *167*, 060501.
- [5] D. Witt, D. Wilde, F. Baakes, F. Belkhir, F. Röder, U. Krewer, *Energy Technol.* **2021**, *9*, 2000989.
- [6] K. A. Severson, P. M. Attia, N. Jin, N. Perkins, B. Jiang, Z. Yang, M. H. Chen, M. Aykol, P. K. Herring, D. Fraggadakis, M. Z. Bazant, S. J. Harris, W. C. Chueh, R. D. Braatz, *Nat. Energy* **2019**, *4*, 383–391.
- [7] J. S. Edge, S. O’Kane, R. Prosser, N. D. Kirkaldy, A. N. Patel, A. Hales, A. Ghosh, W. Ai, J. Chen, J. Yang, S. Li, M. C. Pang, L. Bravo Diaz, A. Tomaszewska, M. W. Marzook, K. N. Radhakrishnan, H. Wang, Y. Patel, B. Wu, G. J. Offer, *Phys. Chem. Chem. Phys.* **2021**, *23*, 8200–8221.
- [8] S. Few, O. Schmidt, G. J. Offer, N. Brandon, J. Nelson, A. Gambhir, *Energy Policy* **2018**, *114*, 578–590.
- [9] E. Peled, S. Menkin, *J. Electrochem. Soc.* **2017**, *164*, A1703–A1719.
- [10] E. Peled, *J. Electrochem. Soc.* **1979**, *126*, 2047–2051.
- [11] S. J. An, J. Li, C. Daniel, D. Mohanty, S. Nagpure, D. L. Wood, *Carbon* **2016**, *105*, 52–76.
- [12] Y. Ali, N. Iqbal, S. Lee, *Int. J. Energy Res.* **2021**, *45*, 5293–5308.
- [13] D. L. Wood, J. Li, C. Daniel, *J. Power Sources* **2015**, *275*, 234–242.
- [14] I. A. Gordon, S. Grugeon, H. Takenouti, B. Tribollet, M. Armand, C. Davoisne, A. Débart, S. Laruelle, *Electrochim. Acta* **2017**, *223*, 63–73.
- [15] S. Malmgren, K. Ciosek, M. Hahlin, T. Gustafsson, M. Gorgoi, H. Rensmo, K. Edström, *Electrochim. Acta* **2013**, *97*, 23–32.
- [16] V. Ramadesigan, K. Chen, N. A. Burns, V. Boovaragavan, R. D. Braatz, V. R. Subramanian, *J. Electrochem. Soc.* **2011**, *158*, A1048.
- [17] F. M. Kindermann, J. Keil, A. Frank, A. Jossen, *J. Electrochem. Soc.* **2017**, *164*, E287–E294.
- [18] M. Heinrich, N. Wolff, N. Harting, V. Laue, F. Röder, S. Seitz, U. Krewer, *Batteries & Supercaps* **2019**, *2*, 530–540.
- [19] F. Single, B. Horstmann, A. Latz, *J. Phys. Chem. C* **2019**, *123*, 27327–27343.
- [20] V. Laue, F. Röder, U. Krewer, *J. Appl. Electrochem.* **2021**, *51*, 1253–1265.
- [21] J. Schmalstieg, C. Rahe, M. Ecker, D. U. Sauer, *J. Electrochem. Soc.* **2018**, *165*, A3799–A3810.
- [22] U. Krewer, M. Christov, T. Vidaković, K. Sundmacher, *J. Electroanal. Chem.* **2006**, *589*, 148–159.
- [23] A. A. Tahmasbi, T. Kadyk, M. H. Eikerling, *J. Electrochem. Soc.* **2017**, *164*, A1307–A1313.
- [24] U. Westerhoff, K. Kurbach, F. Lienesch, M. Kurrat, *Energy Technol.* **2016**, *4*, 1620–1630.
- [25] S. Gantenbein, M. Weiss, E. Ivers-Tiffée, *J. Power Sources* **2018**, *379*, 317–327.
- [26] X. Kong, G. L. Plett, M. S. Trimboli, Z. Zhang, Y. Zheng, *J. Electrochem. Soc.* **2020**, *167*, 013539.
- [27] M.-T. von Srbik, M. Marinescu, R. F. Martinez-Botas, G. J. Offer, *J. Power Sources* **2016**, *325*, 171–184.
- [28] A. Wang, S. Kadam, H. Li, S. Shi, Y. Qi, *npj Comput. Mater.* **2018**, *4*, 15.
- [29] Q. Shi, S. Heng, Q. Qu, T. Gao, W. Liu, L. Hang, H. Zheng, *J. Mater. Chem. A* **2017**, *5*, 10885–10894.
- [30] F. Single, B. Horstmann, A. Latz, *Phys. Chem. Chem. Phys.* **2016**, *18*, 17810–17814.
- [31] Y. Li, K. Leung, Y. Qi, *Acc. Chem. Res.* **2016**, *49*, 2363–2370.
- [32] Q. Zhang, J. Pan, P. Lu, Z. Liu, M. W. Verbrugge, B. W. Sheldon, Y. T. Cheng, Y. Qi, X. Xiao, *Nano Lett.* **2016**, *16*, 2011–2016.
- [33] J. Popovic, *Nat. Commun.* **2021**, *12*, 6240.
- [34] J. Lück, A. Latz, *Phys. Chem. Chem. Phys.* **2016**, *18*, 17799–17804.
- [35] J. Lück, A. Latz, *Phys. Chem. Chem. Phys.* **2018**, *20*, 27804–27821.
- [36] F. Röder, V. Laue, U. Krewer, *Batteries & Supercaps* **2019**, *2*, 248–265.
- [37] J.-M. Chern, F. G. Helfferich, *AIChE J.* **1990**, *36*, 1200–1208.
- [38] O. Borodin, G. V. Zhuang, P. N. Ross, K. Xu, *J. Phys. Chem. C* **2013**, *117*, 7433–7444.
- [39] S. Shi, P. Lu, Z. Liu, Y. Qi, L. G. Hector, H. Li, S. J. Harris, *J. Am. Chem. Soc.* **2012**, *134*, 15476–15487.
- [40] S. Shi, Y. Qi, H. Li, L. G. Hector, *J. Phys. Chem. C* **2013**, *117*, 8579–8593.
- [41] M. Steinhauer, S. Risse, N. Wagner, K. A. Friedrich, *Electrochim. Acta* **2017**, *228*, 652–658.
- [42] R. Drees, F. Lienesch, M. Kurrat, *J. Energy Storage* **2021**, *36*, 102345.
- [43] S. G. Marquis, V. Sulzer, R. Timms, C. P. Please, S. J. Chapman, *J. Electrochem. Soc.* **2019**, *166*, A3693–A3706.
- [44] O. Schmidt, F. Röder, *ACS Appl. Energy Mater.* **2021**, *4*, 4845–4860.
- [45] L. S. Kremer, A. Hoffmann, T. Danner, S. Hein, B. Prifling, D. Westhoff, C. Dreer, A. Latz, V. Schmidt, M. Wohlfahrt-Mehrens, *Energy Technol.* **2020**, *8*, 1900167.
- [46] M. Ender, J. Joos, T. Carraro, E. Ivers-Tiffée, *J. Electrochem. Soc.* **2012**, *159*, A972–A980.
- [47] M. Doyle, T. F. Fuller, J. Newman, *J. Electrochem. Soc.* **1993**, *140*, 1526–1533.
- [48] T. Lombardo, M. Duquesnoy, H. El-Bouysidy, F. Àren, A. Gallo-Bueno, P. B. Jørgensen, A. Bhowmik, A. Demortière, E. Ayerbe, F. Alcaide, M. Reynaud, J. Carrasco, A. Grimaud, C. Zhang, T. Vegge, P. Johansson, A. A. Franco, *Chem. Rev.* (2021) acs.chemrev.1c00108.
- [49] N. Legrand, S. Raël, B. Knosp, M. Hinaje, P. Desprez, F. Lapique, *J. Power Sources* **2014**, *251*, 370–378.
- [50] A. M. Colclasure, R. J. Kee, *Electrochim. Acta* **2010**, *55*, 8960–8973.
- [51] D. K. Karthikeyan, G. Sikha, R. E. White, *J. Power Sources* **2008**, *185*, 1398–1407.
- [52] R. Hausbrand, G. Cherkashinin, H. Ehrenberg, M. Gröting, K. Albe, C. Hess, W. Jaegermann, *Mater. Sci. Eng. B* **2015**, *192*, 3–25.
- [53] A. Tomaszewska, Z. Chu, X. Feng, S. O’Kane, X. Liu, J. Chen, C. Ji, E. Endler, R. Li, L. Liu, Y. Li, S. Zheng, S. Vetterlein, M. Gao, J. Du, M. Parkes, M. Ouyang, M. Marinescu, G. Offer, B. Wu, *eTransportation* **2019**, *1*, 100011.
- [54] A. M. Bizeray, D. A. Howey, C. W. Monroe, *J. Electrochem. Soc.* **2016**, *163*, E223–E229.
- [55] X. Jin, A. Vora, V. Hoshing, T. Saha, G. Shaver, R. E. García, O. Wasynczuk, S. Varigonda, *J. Power Sources* **2017**, *342*, 750–761.
- [56] M. Gabersček, J. Moskon, B. Erjavec, R. Dominko, J. Jamnik, *Electrochem. Solid-State Lett.* **2008**, *11*, 170–174.
- [57] T. P. Heins, N. Harms, L. S. Schramm, U. Schröder, *Energy Technol.* **2016**, *4*, 1509–1513.
- [58] J. P. Schmidt, T. Chrobak, M. Ender, J. Illig, D. Klotz, E. Ivers-Tiffée, *J. Power Sources* **2011**, *196*, 5342–5348.
- [59] J. Landesfeind, H. A. Gasteiger, *J. Electrochem. Soc.* **2019**, *166*, A3079–A3097.
- [60] K. Ushirogata, K. Sodeyama, Y. Okuno, Y. Tateyama, *J. Am. Chem. Soc.* **2013**, *135*, 11967–11974.
- [61] W. Dreyer, J. Jamnik, C. Guhlke, R. Huth, J. Moškon, M. Gaberšček, *Nat. Mater.* **2010**, *9*, 448–453.
- [62] W. Mai, A. Colclasure, K. Smith, *J. Electrochem. Soc.* **2019**, *166*, A1330–A1339.
- [63] Y. Zhuang, Z. Zou, B. Lu, Y. Li, D. Wang, M. Avdeev, S. Shi, *Chin. Phys. B* **2020**, *29*, 068202.
- [64] M. Ender, *J. Power Sources* **2015**, *282*, 572–580.
- [65] F. Röder, S. Sonntag, D. Schröder, U. Krewer, *Energy Technol.* **2016**, *4*, 1588–1597.
- [66] J. Costard, M. Ender, M. Weiss, E. Ivers-Tiffée, *J. Electrochem. Soc.* **2017**, *164*, A71–A79.
- [67] E. Prada, D. Di Domenico, Y. Creff, J. Bernard, V. Sauviant-Moynot, F. Huet, *J. Electrochem. Soc.* **2013**, *160*, A616–A628.
- [68] C. Nowak, L. Froboese, M. Winter, T. Placke, W. Haselrieder, A. Kwade, *Energy Technol.* **2019**, *7*, 1900528.
- [69] J. Maibach, F. Lindgren, H. Eriksson, K. Edström, M. Hahlin, *J. Phys. Chem. Lett.* **2016**, *7*, 1775–1780.

- [70] T. Momma, M. Matsunaga, D. Mukoyama, T. Osaka, *J. Power Sources* **2012**, *216*, 304–307.
- [71] M. Ecker, S. Käbitz, I. Laresgoiti, D. U. Sauer, *J. Electrochem. Soc.* **2015**, *162*, A1849–A1857.
- [72] T. Li, X.-Z. Yuan, L. Zhang, D. Song, K. Shi, C. Bock, *Electrochem. Energy Rev.* **2020**, *3*, 43–80.
- [73] W. Liu, P. Liu, D. Mitlin, *Adv. Energy Mater.* **2020**, 2002297.
- [74] L. Liu, J. Park, X. Lin, A. M. Sastry, W. Lu, *J. Power Sources* **2014**, *268*, 482–490.
- [75] R. D. Deshpande, D. M. Bernardi, *J. Electrochem. Soc.* **2017**, *164*, A461–A474.
- [76] L. Bläubaum, P. Röse, L. Schmidt, U. Krewer, *ChemSusChem* **2021**, cssc.202100845.
- [77] C. H. Lee, J. A. Dura, A. LeBar, S. C. DeCaluwe, *J. Power Sources* **2019**, *412*, 725–735.
- [78] C. Stetson, T. Yoon, J. Coyle, W. Nemeth, M. Young, A. Norman, S. Pylypenko, C. Ban, C. S. Jiang, M. Al-Jassim, A. Burrell, *Nano Energy* **2019**, *55*, 477–485.
- [79] P. Verma, P. Maire, P. Novák, *Electrochim. Acta* **2010**, *55*, 6332–6341.
- [80] W. Huang, J. Wang, M. R. Braun, Z. Zhang, Y. Li, D. T. Boyle, P. C. McIntyre, Y. Cui, *Matter* **2019**, *1*, 1232–1245.
- [81] D. R. Kim, J. W. Kang, T. H. Eom, J. M. Kim, J. Lee, C. Y. Won, *Appl. Sci.* **2018**, *8*, 1–12.
- [82] M. Ender, J. Joos, A. Weber, E. Ivers-Tiffée, *J. Power Sources* **2014**, *269*, 912–919.
- [83] K. Ushirogata, K. Sodeyama, Z. Futera, Y. Tateyama, Y. Okuno, *J. Electrochem. Soc.* **2015**, *162*, A2670–A2678.
- [84] F. Röder, R. D. Braatz, U. Krewer, *J. Electrochem. Soc.* **2017**, *164*, E3335–E3344.
- [85] M. Tang, S. Lu, J. Newman, *J. Electrochem. Soc.* **2012**, *159*, A1775–A1785.
- [86] Y. Wang, S. Nakamura, M. Ue, P. B. Balbuena, *J. Am. Chem. Soc.* **2001**, *123*, 11708–11718.
- [87] T. Osaka, T. Momma, D. Mukoyama, H. Nara, *J. Power Sources* **2012**, *205*, 483–486.
- [88] A. Tahmasbi, M. Eikerling, *Electrochim. Acta* **2018**, *283*, 75–87.
- [89] S. Xia, L. Mu, Z. Xu, J. Wang, C. Wei, L. Liu, P. Pianetta, K. Zhao, X. Yu, F. Lin, Y. Liu, *Nano Energy* **2018**, *53*, 753–762.
- [90] Y. Shi, M. Zhang, D. Qian, Y. S. Meng, *Electrochim. Acta* **2016**, *203*, 154–161.
- [91] N. Harting, N. Wolff, U. Krewer, *Electrochim. Acta* **2018**, *281*, 378–385.

Manuscript received: February 4, 2022
Revised manuscript received: March 14, 2022
Accepted manuscript online: March 22, 2022
Version of record online: May 19, 2022